Exotic shape symmetries around the fourfold octupole magic number $N = 136$: Formulation of experimental identification criteria

J. Yang [1,2] J. Dudek [3,*] I. Dedes [4] A. Baran [2] D. Curien [3] A. Gaamouci [5] A. Góźdź [2] A. Pędrak [6] D. Rouvel,[3] H. L. Wang [1] and J. Burkat [7]

[1]*School of Physics and Microelectronics, Zhengzhou University, Zhengzhou 450001, China*
[2]*Institute of Physics, Marie Curie-Skłodowska University, PL-20 031 Lublin, Poland*
[3]*Université de Strasbourg, CNRS, IPHC UMR 7178, F-67 000 Strasbourg, France*
[4]*Institute of Nuclear Physics, Polish Academy of Sciences, PL-31 342 Kraków, Poland*
[5]*Laboratoire de Physique Théorique, Faculté de Physique, USTHB, BP 32, El Alia, 16111 Bab Ezzouar, Algiers, Algeria*
[6]*National Centre for Nuclear Research, Theoretical Physics Division, Pl-02-093 Warsaw, Poland*
[7]*Brasenose College, University of Oxford, Oxford OX1 4AJ, United Kingdom*

(Received 1 February 2022; accepted 21 March 2022; published 31 March 2022)

We employ a realistic nuclear mean-field theory using the phenomenological, Woods-Saxon Hamiltonian with newly adjusted parameters containing no parametric correlations; originally present correlations are removed employing the Monte Carlo approach. We find very large neutron shell gaps at $N = 136$ for all the four octupole deformations $\alpha_{3\mu=0,1,2,3}$. These shell gaps generate well-pronounced double potential-energy minima in the standard multipole $(\alpha_{20}, \alpha_{22}, \alpha_{3\mu}, \alpha_{40})$ representation, often at $\alpha_{20} = 0$, which in turn generate exotic symmetries C_{2v}, D_{2d}, T_d, and D_{3h}, discussed in detail. The main goal of the article is to formulate spectroscopic criteria for experimental identification. Calculations employing macroscopic-microscopic method are performed for nuclei with $Z \geqslant 82$ and $N \geqslant 126$ in multidimensional deformation spaces to analyze the expected exotic symmetries and octupole shape instabilities in the mass table "northeast" of the doubly magic ^{208}Pb nucleus. Whereas the proton-unperturbed properties of neutron-generated octupole shell effects are illustrated in detail for exotic $_{Z=82}\mathrm{Pb}_{N>126}$ nuclei, our discussion is extended into even-even $Z > 82$ nuclei approaching the less exotic Z/N ratios, to encourage experiments which could identify the predicted exotic symmetries. In addition to the tetrahedral point group symmetry, T_d, of which experimental evidence has recently been published, we present D_{2d} symmetry resulting from a superposition of axially symmetric quadrupole and tetrahedral symmetries and two new point group symmetries, D_{3h} and C_{2v}, associated with the octupole α_{33} and α_{31} energy minima, respectively. The multidimensional $n > 2$ deformation spaces are treated as usual by projecting the total potential energies onto the $n = 2$ subspace. Using the representation theory of point groups we formulate quantum mechanical criteria for experimental identification of exotic symmetries through analysis of the specific properties of the collective rotational bands generated by the symmetries. The resulting band structures happen to be markedly distinct from the structure of the bands generated by ellipsoidal symmetry quantum rotors; those various rotational properties are discussed in detail.

DOI: 10.1103/PhysRevC.105.034348

I. INTRODUCTION

Nuclei with the strongest binding energies, whose proton and neutron numbers are equal to one of the "magic" numbers (corresponding to the fully occupied spherical shells with Z_0 and N_0 taken as 8, 20, 28, 50, 82, 126) can be considered as ideally spherical. Adding (or removing) a few extra nucleons to these spherical cores will immediately cause nonspherical shape polarizations to appear. With just a few such particle or hole states activated, to first order, axial-symmetry quadrupole-shape distortions appear. At first, one might consider them negligible. Indeed, the numerical values of the involved quadrupole deformations, $\alpha_{20} \in [-0.02, 0.02]$ or so, generate surfaces which, to the "naked eye," remain undistinguishable from the ideal sphere. Yet, neglecting them could lead to significant errors since the corresponding nucleon energies may vary up to ± 1 MeV for $i_{13/2}$ and its neighboring orbitals of high j, high m_j (nucleon angular momentum and its projection on the symmetry axis); see, e.g., Ref. [1] and references therein.

The concept of nuclear shapes and shape coexistence has attracted the attention of researchers over decades of the previous and present centuries; see, e.g., reviews in Refs. [2–4] and references therein. With nucleon numbers departing from the spherical-closure Z_0 and N_0 values, the nucleon level densities at energies close to the Fermi energies increase significantly for spherical shapes. This, in turn, leads to a strong increase of what in the language of nuclear mean-field theory are referred to as "shell energies." As a consequence, an expulsion of the

*Corresponding author: Jerzy.Dudek@iphc.cnrs.fr

nuclei in question from the spherical shape regions to those of significant deformation away or even far away from spherical symmetry takes place.

In terms of the mean-field theory modeling, both the phenomenological microscopic-macroscopic methods of Strutinsky and Hartree-Fock, or Hartree-Fock-Bogolyubov, lead to a number of competing potential energy minima generally corresponding to nonspherical shapes with significant local equilibrium energy differences, often separated by significant potential energy barriers. This mechanism has opened the way to numerous studies of the so-called shape isomers, as well as shape evolution as the consequence of exciting nuclei in experiments, by transferring angular momentum or by increasing the nuclear temperature.

In this article we will focus on examining the competing total energy minima of distinct geometrical forms. We will not address the frequently discussed subject of the so-called prolate-oblate shape coexistence, referring to configurations with two minima separated by a barrier, one corresponding, to the positive quadrupole deformation ($\alpha_{20} > 0$, prolate) and the other to the negative one ($\alpha_{20} < 0$, oblate). Instead, we will focus on predictions addressing exotic shapes, whose symmetry properties will be described mathematically using group theory.

To build up a link between the shape properties described within the mean-field theory approach and the symmetry properties treated with the help of point group theory it will be convenient to introduce the usual multipole expansion of the nuclear surface, Σ, in a standard manner in terms of the spherical harmonics, $Y_{\lambda\mu}(\vartheta, \varphi)$:

$$\Sigma: \quad R(\vartheta, \varphi) = R_0 c(\alpha)\left[1 + \sum_{\lambda\mu} \alpha^*_{\lambda\mu} Y_{\lambda\mu}(\vartheta, \varphi)\right]. \tag{1}$$

The expansion coefficients $\alpha_{\lambda\mu}$ in Eq. (1) are usually called "deformation parameters" or "deformations" in short. They are generally complex but we limit ourselves, as many other authors do, to the real parametrization. The radius parameter $R_0 \equiv r_0 A^{1/3}$, where $r_0 \approx 1.2$ fm, gives an approximation of the effective nuclear spherical radius in Fermi, and the auxiliary function $c(\alpha)$ assures that the volume encompassed by the surface is constant and independent of deformation.

Calculations confirmed by experiment indicate that the typical lowest order equilibrium deformations involve quadrupole ($\lambda = 2$) components, axial α_{20} and nonaxial α_{22}, often accompanied by smaller but persisting axial hexadecapole ($\lambda = 4$) deformation, α_{40}. It was found long ago that, in certain areas of the nuclear mass table, this characteristic behavior is modified by octupole ($\lambda = 3$) axial ($\mu = 0$) pear-shape contributions with a nonvanishing deformation α_{30}; see, e.g., early articles in Refs. [5–7] indicating the presence of the "octupole magic numbers": 32, 40, 56, 90, 136, as discussed in more detail in the next section; see also Ref. [8].

Other multipolarities or their combinations will be referred to as exotic. In particular, the recently discovered [9] nuclear tetrahedral and octahedral symmetries can be represented with the help of nuclear surfaces in which deformation parameters enter in the appropriately predefined combinations of certain multipolarities, λ. For instance, tetrahedrally symmetric surfaces, within what we refer to as the first-order deformation parameter, t_1, involve only the nonaxial octupole deformation parameters $\alpha_{3\pm2}$. For the next allowed order, referred to as the second-order deformation parameter t_2, one would need a combination of two deformation parameters with the order $\lambda = 7$, Ref. [10]:

$$t_1 \equiv \alpha_{3\pm2}, \tag{2}$$

$$t_2 \equiv \alpha_{7\pm2} \quad \text{and} \quad \alpha_{7\pm6} = -\sqrt{11/13}\,\alpha_{7\pm2}. \tag{3}$$

Similarly (see Ref. [10]), for the second lowest order octahedral symmetry deformations o_1 and o_2, one needs combinations of $\lambda = 4$ and $\lambda = 6$ multipolarities as follows:

$$o_1 \equiv \alpha_{40} \quad \text{and} \quad \alpha_{4\pm4} = -\sqrt{5/14}\,\alpha_{40}, \tag{4}$$

$$o_2 \equiv \alpha_{60} \quad \text{and} \quad \alpha_{6\pm4} = +\sqrt{7/2}\ \alpha_{60}. \tag{5}$$

As far as the construction of experimental symmetry identification criteria is concerned, the mathematical treatment of the exotic symmetries, which will be discussed in the present article, follows exactly the treatment tested earlier in Ref. [11] and applied in Ref. [9].

In what follows we will be particularly interested in the impact of nonaxial octupole shape components $\alpha_{3\mu\neq0}$ on the total potential energy in heavy nuclei. Mean-field calculations indicate two characteristic scenarios. One of them involves the presence of octupole shape components superposed with nonzero quadrupole ones, $\alpha_{20} \neq 0$. This scenario can be considered well known, as one can conclude from the numerous articles published on this subject, such as Refs. [5–7] or the more recent ones Refs. [12,13], and references therein; see also Refs. [14–16] as well as the discussions focused on heavy nuclei, Refs. [17,18]. The reader interested in the early studies of the related mean-field shell effects in superdeformed nuclei is invited to consult Refs. [19,20]; similarly, those interested in high-spin evolution thereof should see Refs. [21,22].

The other scenario involves pure octupole instabilities, ($\alpha_{20} = 0, \alpha_{3\mu} \neq 0$), which evolve in certain nuclei with varying nucleon numbers. Despite the apparent similarities between the two scenarios with and without vanishing α_{20} quadrupole deformation, the resulting point group symmetries as well as their possible experimental manifestations are generally distinct and will be discussed in this article.

It turns out that heavy nuclei are particularly predisposed to produce pronounced octupole shape effects. Among them, certain Pb isotopes seem particularly attractive to us, as they allow one to focus on studying a relatively clean buildup of those shape polarizations *caused by neutrons, while keeping the protons within the shell closure* $Z = 82$. Our detailed calculations predict numerous cases of coexistence of competing local equilibrium deformations with all four nonvanishing octupole components, which naturally raises questions about the potential energy barriers separating such local energy minima, as well as other nuclear structure implications discussed later in this article.

Our calculations involve nuclear shape analysis in the spaces of quadrupole (α_{20} and α_{22}) variables and octupole variables $\alpha_{3\mu}$ with $\mu = 0, 1, 2, 3$, accompanied occasionally by some extra test projections involving more exotic

multipolarities (λ, μ), but the bulk properties are analyzed in the four-dimensional (4D) deformation subspaces in this article.

Section II will be devoted to a brief description of the structure of the nuclear Hamiltonian used in this article together with typical total energy calculation results relevant for the nuclear range studied. This will bring us to the subject of Sec. III, in which the characteristic shape-competition properties predicted on the basis of microscopic calculations of the potential energies in exotic heavy Pb nuclei will be extended to nuclei with $Z > 82$, which are easier to access experimentally with the presently available projectile-target combinations, facilitating new propositions of exotic-symmetry identification experiments.

In Sec. IV we will formulate quantum criteria which allow for an experimental identification of exotic point group symmetries introduced earlier, with the help of characteristic rotational "molecular symmetry bands." Since their properties generally differ drastically from the properties of the well-known bands generated by the ellipsoidal quantum rotors, dominated by $(\Delta I = 2)$ transitions, the corresponding information will allow for formulating experimental proposals for exotic symmetry identification in unique manners.

The summary and conclusions will be presented in Sec. V.

II. NUCLEAR MEAN-FIELD HAMILTONIAN: DEFINITIONS AND TYPICAL RESULTS

The nuclear potential energy calculations presented in this article were performed with the help of the macroscopic-microscopic method of Strutinsky [23,24], employing the recently reanalyzed "universal" parametrization of the deformed Woods-Saxon potential [25]. The idea of "universality" was introduced long ago in the presently used context in Ref. [26]; see also Ref. [27] for contemporary links. The adjective "universal" refers to the fact that a unique parameter set is used for all the nuclei in the entire mass table.

A. Mean-field Hamiltonian and nuclear potential energy

We recall briefly the definition of the nuclear mean-field Woods-Saxon Hamiltonian, which can be considered very standard today:

$$\hat{H}_{WS} = \hat{T} + \hat{\mathcal{V}}_{WS} + \hat{\mathcal{V}}^{\rm so}_{WS} + [\hat{\mathcal{V}}_{\rm Coulomb} \text{ for protons}], \quad (6)$$

where $\hat{T}$ represents the nucleonic kinetic energy operator and $\hat{\mathcal{V}}_{WS}$ the central Woods-Saxon potential, the latter defined with the help of the equation of the nuclear surface, Σ, as follows:

$$\hat{\mathcal{V}}_{WS}(\vec{r}, \alpha; V^{\rm c}, r^{\rm c}, a^{\rm c}) = \frac{V^{c}}{1 + \exp[{\rm dist}_{\Sigma}(\vec{r}, R^{c}; \alpha)/a^{c}]}. \quad (7)$$

The symbols introduced above have the following meaning: $V^{\rm c}$ is the central potential depth parameter, $r^{\rm c}$ (in $R^{\rm c} = r^{\rm c}A^{1/3}$) the central radius parameter, and $a^{\rm c}$ the central-potential diffusivity parameter. The function ${\rm dist}_{\Sigma}(\vec{r}, R^{\rm c}; \alpha)$ represents the geometrical distance between the nucleon position $\vec{r} \equiv \{x, y, z\}$ and the nuclear surface Σ, whereas α stands for all the deformation parameters $\alpha_{\lambda\mu}$.

The spin-orbit potential as usual involves the gradient of the central one,

$$\hat{\mathcal{V}}^{\rm so}_{WS}(\vec{r}, \hat{p}, \hat{s}, \alpha; \lambda^{\rm so}, r^{\rm so}, a^{\rm so}) = \frac{2\hbar\lambda^{\rm so}}{(2mc)^2}\left[\left(\vec{\nabla}V^{\rm so}_{WS}\right) \wedge \hat{p}\right] \cdot \hat{s}, \quad (8)$$

where

$$V^{\rm so}_{WS}(\vec{r}, \alpha; V^{\rm c}, r^{\rm so}, a^{\rm so}) = \frac{V^{c}}{1 + \exp[{\rm dist}_{\Sigma}(\vec{r}, R^{\rm so}; \alpha)/a^{\rm so}]}. \quad (9)$$

We have introduced $\lambda^{\rm so}$ as a dimensionless spin-orbit strength scaling factor, $r^{\rm so}$ (in $R^{\rm so} = r^{\rm so}A^{1/3}$) as the spin-orbit radius, and $a^{\rm so}$ as the spin-orbit diffusivity parameter.

In principle, this definition of the phenomenological mean-field Hamiltonian with the deformation-dependent Woods-Saxon proton and neutron potentials explicitly introduces two sets of six parameters each,

$$\left\{V^{\rm c}_{\pi,\nu}, r^{\rm c}_{\pi,\nu}, a^{\rm c}_{\pi,\nu}; \lambda^{\rm so}_{\pi,\nu}, r^{\rm so}_{\pi,\nu}, a^{\rm so}_{\pi,\nu}\right\}, \quad (10)$$

one for protons π and one for neutrons ν. However, it turns out that an alternative representation of the parameters of the Hamiltonian in question that explicitly involves a smooth dependence on Z and N is significantly better suited for large scale calculations. The interested reader may consult Ref. [25] for details, here we will limit ourselves to recapitulating the final results based on the above reference.

The mean-field Hamiltonian parameters used in the present article have been adjusted in Ref. [25] to the empirical single-nucleon energies established for the doubly magic spherical nuclei

$$^{16}{\rm O},\ ^{40}{\rm Ca},\ ^{48}{\rm Ca},\ ^{56}{\rm Ni},\ ^{90}{\rm Zr},\ ^{132}{\rm Sn},\ ^{146}{\rm Gd},\ ^{208}{\rm Pb}, \quad (11)$$

following the evaluation of Ref. [28]. When adjusting parameters to the data on several nuclei (eight in the present case) it will be of significant advantage to introduce explicitly the isospin dependence in the strength parameters of central and spin-orbit potentials in the form directly involving the isospin strength constants κ as follows:

$$V^{\rm c}_{\pi,\nu} = V^{\rm c}_{0}\left(1 \pm \kappa^{\rm c}\frac{N-Z}{N+Z}\right) \quad (12)$$

and

$$\lambda^{\rm so}_{\pi,\nu} = \lambda^{\rm so}_{0}\left(1 \pm \kappa^{\rm so}\frac{N-Z}{N+Z}\right), \quad (13)$$

with the plus sign holding for the protons and the minus sign for the neutrons. According to this modification, $V^{\rm c}_0$, $\lambda^{\rm so}_0$, as well as $\kappa^{\rm c}$ and $\kappa^{\rm so}$ are new adjustable constants, corresponding to the ones introduced originally, and we can formally write an equivalence relation between the two subsets:

$$\left\{V^{\rm c}_{0}, \kappa^{\rm c}; \lambda^{\rm so}_{0}, \kappa^{\rm so}\right\} \leftrightarrow \left\{V^{\rm c}_{\pi}, V^{\rm c}_{\nu}; \lambda^{\rm so}_{\pi}, \lambda^{\rm so}_{\nu}\right\}. \quad (14)$$

From contemporary research results one expects that modeling uncertainties should be tested and controlled before submitting for publications; see, e.g., the *Physical Review* Editorial, Ref. [29]. One of the first, most direct verifications in this context consists of establishing the possible presence (or absence) of the parametric correlations generated by the newly parametrized Hamiltonians. This requirement is fundamental since one may demonstrate rigorously that Hamiltonians with

TABLE I. Parameters of the universal Woods-Saxon Hamiltonian from Ref. [25]. Upper row: protons. Lower row: neutrons. The dependent parameters resulting from the procedure of elimination of the parametric correlations are $r_\pi^c = 1.278$ fm, $r_\nu^c = 1.265$ fm, $r_\pi^{so} = 0.830$ fm, $r_\nu^{so} = 0.890$ fm. The spin-orbit diffusivity parameters are $a_\pi^{so} = a_\nu^{so} = 0.700$ fm; see Ref. [25].

	V_0^c (MeV)	κ^c	$a_{\pi,\nu}^c$ (fm)	λ_0^{so}	κ^{so}
Mean values	−50.225	0.624	0.594 0.572	26.210	−0.683
Standard error	0.142	0.013	0.010 0.011	0.513	0.139

parametric correlations have essentially null predictive power for the data outside of the fitting zone; see, e.g., Secs. III and IV of Ref. [25] and references therein.

In the present project, the well-established tools of the inverse problem theory of applied mathematics have been employed. By applying standard mathematical algorithms, which involve among others Monte Carlo simulations, the presence of parametric correlations for 4 out of 12 originally introduced Woods-Saxon parameters [see Eq. (10)] has been detected. The identified correlations have been removed so that the final parameter set contains only eight independent ones. The corresponding results from [25] are collected in Table I.

The Schrödinger equation with the Hamiltonian of Eq. (6) is solved using standard diagonalization methods with a matrix representation of the Hamiltonian within the anisotropic harmonic oscillator (HO) basis. The HO basis cutoff conditions have been adjusted in such a way that the calculated single-nucleon energies remain stable within three decimal places even for the extreme ranges of variations of the deformation parameters; see Ref. [25] for details.

The total potential energies are calculated using the macroscopic-microscopic method of Strutinsky as in Refs. [23,24]. In accordance with the corresponding definitions and notation the nuclear potential energy is calculated as

$$E_{\text{total}} = E_{\text{macro}} + \delta E^{\pi}_{\text{micro}} + \delta E^{\nu}_{\text{micro}}. \tag{15}$$

The first term stands for the classical macroscopic liquid-drop model contribution and the two microscopic terms are defined as the sums of the so-called shell correction and pairing correction terms introduced in Refs. [23,24].

To calculate the nuclear energies we employ a macroscopic energy description in the form of the finite-range liquid-drop model (FRLDM). It contains the surface energy term given by the Yukawa-plus-exponential finite-range model of Ref. [30] within the formulation of Refs. [31,32]. Our macroscopic energy expression coincides with Eq. (62) of Ref. [33]. All other terms in the Strutinsky energy expressions are standard, and the interested reader may consult Ref. [25] and the references therein.

B. Deformed mean-field shell effects in 4D octupole space

We begin our presentation of the octupole shape susceptibilities in heavy lead isotopes and the neighboring heavy nuclei by first focusing on the strongest gaps in the single-particle spectra, which result from an increase of the octupole deformations $\alpha_{3\mu}$ for $\mu = 0$, 1, 2, and 3. We use the Hamiltonian in its parametric correlation-free form introduced in the preceding section, and begin with the "traditional," pear-shape, axially symmetric deformation α_{30}. The corresponding illustration is given in Fig. 1.

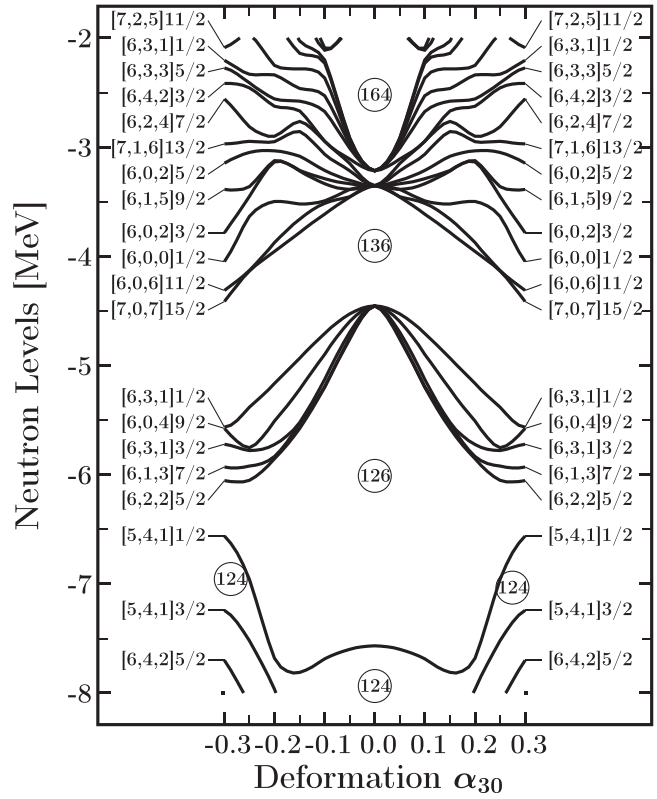

FIG. 1. Single-particle neutron levels as functions of the pear-shape axial octupole deformation obtained with the Universal Woods-Saxon Hamiltonian. The pear-shape deformations are the earliest studied in the literature. The "magic" octupole number $N = 136$ deserves notice; for details see the text.

The α_{30} octupole shell opening at $N = 136$ is clearly visible above the $2g_{9/2}$ orbital, separating the $N = 126$ and $N = 136$ spherical-shell gaps with its five doubly degenerate members $m_j = \pm\frac{1}{2}, \pm\frac{3}{2}, \ldots, \pm\frac{9}{2}$ downsloping between $\alpha_{30} = 0$ and $\alpha_{30} \approx \pm 0.3$. The observed gap is caused by a repulsive interaction between the $2g_{9/2}$ orbital members from the main $N = 6$ shell and the $1j_{15/2}$ intruder orbital members from the main $N = 7$ shell. The presence of the strong gaps at $N = 136$ in all four octupole shape components $\mu = 0, 1, 2, 3$ can be traced back to the strong coupling via octupole operators,

$$\hat{Q}_{3\mu} \propto r^3 Y_{3\mu}, \tag{16}$$

entering the octupole-octupole residual interaction Hamiltonian "sandwiched" between the *bra* and the *ket* states originating from the $1j_{15/2}$ and $2g_{9/2}$ orbitals. They differ in terms of the orbital angular momentum quantum numbers by $\Delta\ell = \lambda = 3$ (for the microscopic origin underlying the mechanisms mentioned, see Refs. [34,35]).

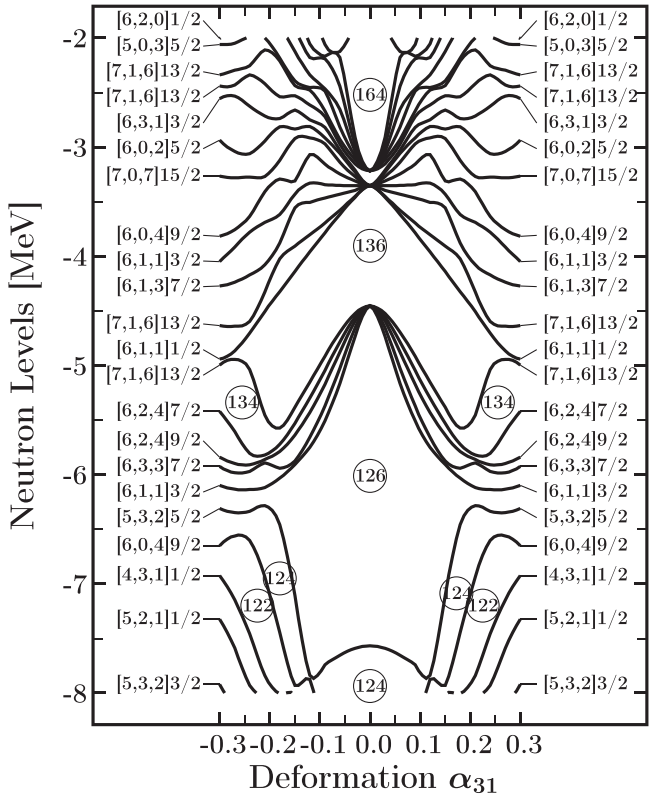

FIG. 2. Similar to the preceding figure, but for the α_{31} octupole deformation. The α_{31} octupole gap at $N = 136$ extends only to ± 0.20.

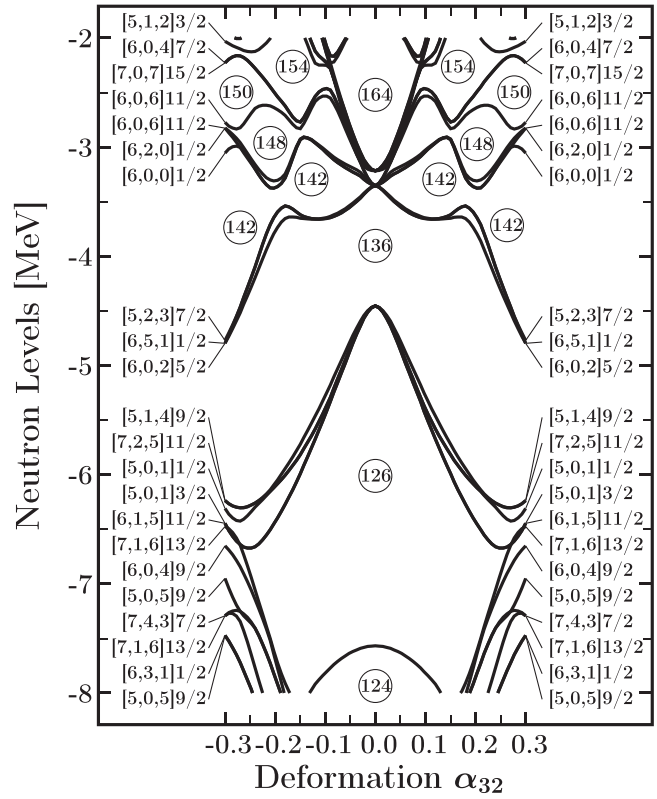

FIG. 3. Similar to the preceding figures, here for the α_{32} deformation representing a very exotic tetrahedral symmetry, whose double point group possesses 48 symmetry elements. Particularly strong shell-gap openings at $N = 136$ and $N = 142$ deserve attention.

Figure 2 shows a qualitatively similar behavior of the single-particle levels, even though the α_{31} octupole gap at $N = 136$ is slightly less pronounced. Its microscopic origin can be traced back to the properties of the octupole operator in Eq. (16) and the $\Delta\ell = 3$ *bra* vs *ket* relations; see Eq. (C.1) of Ref. [34].

In the case of the α_{32} octupole deformation effect illustrated in Fig. 3 we must expect the strongest shell effects due to the fact that this particular degree of freedom *de facto* represents the tetrahedral symmetry; see Ref. [9] and references therein. As is well known from group theory, among the irreducible representations of the double-tetrahedral group T_d^D applicable in the discussed case of the Fermion mean-field Hamiltonian we find one four-dimensional irreducible representation (the corresponding levels carry fourfold degeneracies and are characterized by the double Nilsson labels in Fig. 3) and two two-dimensional ones. The fourfold degeneracies of single-particle levels lead to an increase in the average level spacings, and occasionally to bigger shell gaps. Indeed, we find that the $N = 136$ octupole gaps are the strongest in the discussed tetrahedral symmetry case, which is clearly visible from the comparison of Figs. 1–4. Moreover, we find the two most significant α_{32} deformed gaps at $N = 136$ and $N = 142$, the size of the former close in its energy scale to the size of the spherical $N = 126$ gap.

Another manifestation of the $N = 136$ gap in the case of the α_{33} octupole deformation is visible in Fig. 4.

Comparing all four illustrations presenting the single-neutron orbitals as functions of the octupole deformations $\alpha_{3\mu}$ with $\mu = 0, 1, 2, 3$, we may conclude that, according to the discussion in the text neighboring Eq. (16), the repulsion of the $2g_{9/2}$ vs $1j_{15/2}$ orbitals transmitted via $\hat{Q}_{\lambda=3}$ operators leads to the strong shell gaps at the neutron number $N = 136$ for all four components of the octupole tensor; see Eq. (C.1) of Ref. [34] for explicit forms of the relevant matrix elements. The strongest effect can be attributed to α_{32} deformation generating tetrahedral symmetry, whose specific mechanism is due to the reasons based on the group theoretical arguments, as qualitatively discussed above.

C. Octupole structure of the nuclear potential energies

We proceed to examining the impact of the single-nucleon octupole gaps illustrated in the preceding section on the nuclear potential energies. We will be particularly interested in the accompanying mechanisms, such as the presence of multiple potential energy minima and the barriers separating them, the fission barriers, and the appearance of flat energy zones resembling valleys. The latter often give rise to a lowering of the collective vibrational nuclear energies. The single-particle energy diagrams presented in the preceding section allow for a qualitative overview of the global properties of underlying shell effects, but otherwise can hardly be used for direct

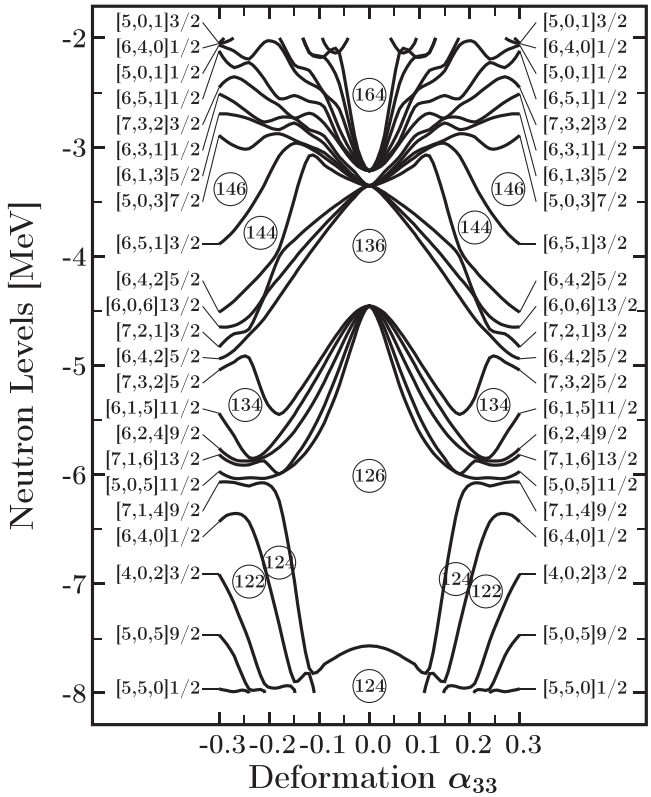

FIG. 4. Similar to the preceding cases, here for the octupole α_{33} deformation. Observe the presence of octupole gaps at $N = 136$ and $N = 146$.

comparison, e.g., as leading to spectroscopic experimental information.

We will present a series of total potential energy illustrations divided into two smaller subsequences. In the first one we wish to show how the octupole susceptibilities evolve with the neutron number, beginning with $N = 126$ up to $N = 136$; the latter playing a role of a 'universal octupole magic number," or, alternatively 'fourfold octupole magic number," to all four octupole deformations α_{30}, α_{31}, α_{32}, and α_{33}, simultaneously.

It turns out that all the four corresponding types of octupole-quadrupole potential energy projections, i.e., (α_{30} vs α_{20}), (α_{31} vs α_{20}), (α_{32} vs α_{20}), and (α_{33} vs α_{20}) look quite similar to each other. We will only show the (α_{30} vs α_{20}) projections as representative examples. They are obtained as the results of four-dimensional calculations: at each point of every one of the mentioned 2D projections a minimization is performed over the triaxial-quadrupole deformation α_{22} and the hexadecapole deformation α_{40}.

The results illustrating arrival of stable, strongly pronounced octupole minima with increasing neutron number are shown in Fig. 5 presenting three nuclei: ^{208}Pb$_{126}$, ^{212}Pb$_{130}$, and ^{216}Pb$_{134}$. The first of them manifests a flat "north-south" valley along the α_{30} axis. The second shows the onset of the double-minimum pear-shape octupole structures. The third manifests two fully developed symmetric octupole minima, separated by a potential barrier of over 2 MeV.

The maps involving alternative multipolarities α_{31}, α_{32}, and α_{33} manifest a very similar behavior, and are not shown.

We find it instructive to present instead the sequence of all four α_{20} vs $\alpha_{3\mu}$ projections for the magic configuration $N = 136$, i.e., for the ^{218}Pb$_{136}$ nucleus; see Fig. 6. Comparison shows that the highest barriers separating the twin octupole minima correspond to tetrahedral symmetry α_{32}, the height exceeding 3 MeV, and pear-shape symmetry α_{30}, with the barrier clearly in excess of 2 MeV.

Yet, the remaining deformations α_{30}, α_{31}, and α_{33} produce very well-pronounced separation barriers as well. All projections predict the coexistence of the well pronounced superdeformed minima, at 4–5 MeV relative height (depending slightly on the projection chosen).

Results in Fig. 6 show that the fission properties will be determined by the mass-asymmetry pear-shape evolution at increasing elongation since the corresponding fission barriers are significantly lower in this case. For the $\alpha_{3\mu\neq 0}$ projections the predicted saddle points remain axially symmetric at $\alpha_{3\mu\neq 0} = 0$.

III. EXOTIC SYMMETRIES: FROM HEAVY Pb ISOTOPES TO $Z > 82$ NUCLEI

Heavy isotopes of lead, $_{82}$Pb$_{N\geqslant 126}$, were selected for our study of exotic nuclear shape properties for a number of reasons. It will be instructive to list them explicitly before proceeding with the next steps of the presentation. However, as the isotopes represent relatively exotic species, the corresponding experimental data are limited, or scarce. In order to encourage effective experimental efforts to identify the underlying exotic symmetries in question it will be instructive to enlarge the discussion to also cover some of the more accessible nuclei. Keeping this in mind, as well as the fact that the symmetry effects introduced evolve in a multifold manner, they will need to be discussed in some detail for $Z > 82$ nuclei.

A. Unique structural features of heavy Pb isotopes as the theory test ground

The octupole effects, appearing in the discussed lead nuclei in their pure form, i.e., at vanishing quadrupole deformation, evolve with Z into more complex structures. First, in several nuclei the α_{30} and α_{31} susceptibilities occurring at $\alpha_{20} = 0$ evolve into octupole valleys superposed with nonzero quadrupole deformations $\alpha_{20} \neq 0$, as seen from Figs. 7 and 8.

One may expect that this evolution with increasing Z gives rise to "traditional" octupole-type rotational patterns combined with low-lying octupole oscillation structures also in heavier nuclei.

Second, and perhaps more importantly, the octupole components α_{32} and α_{33}—while generating valley patterns similar to the ones just described—produce simultaneously well-defined double minima at $\alpha_{20} = 0$. The latter are separated from the lower-lying quadrupole minima by significant barriers and imply in a way parallel shape coexistence patterns. On the one hand, collective octupole bands build on the $\alpha_{20} \neq 0$

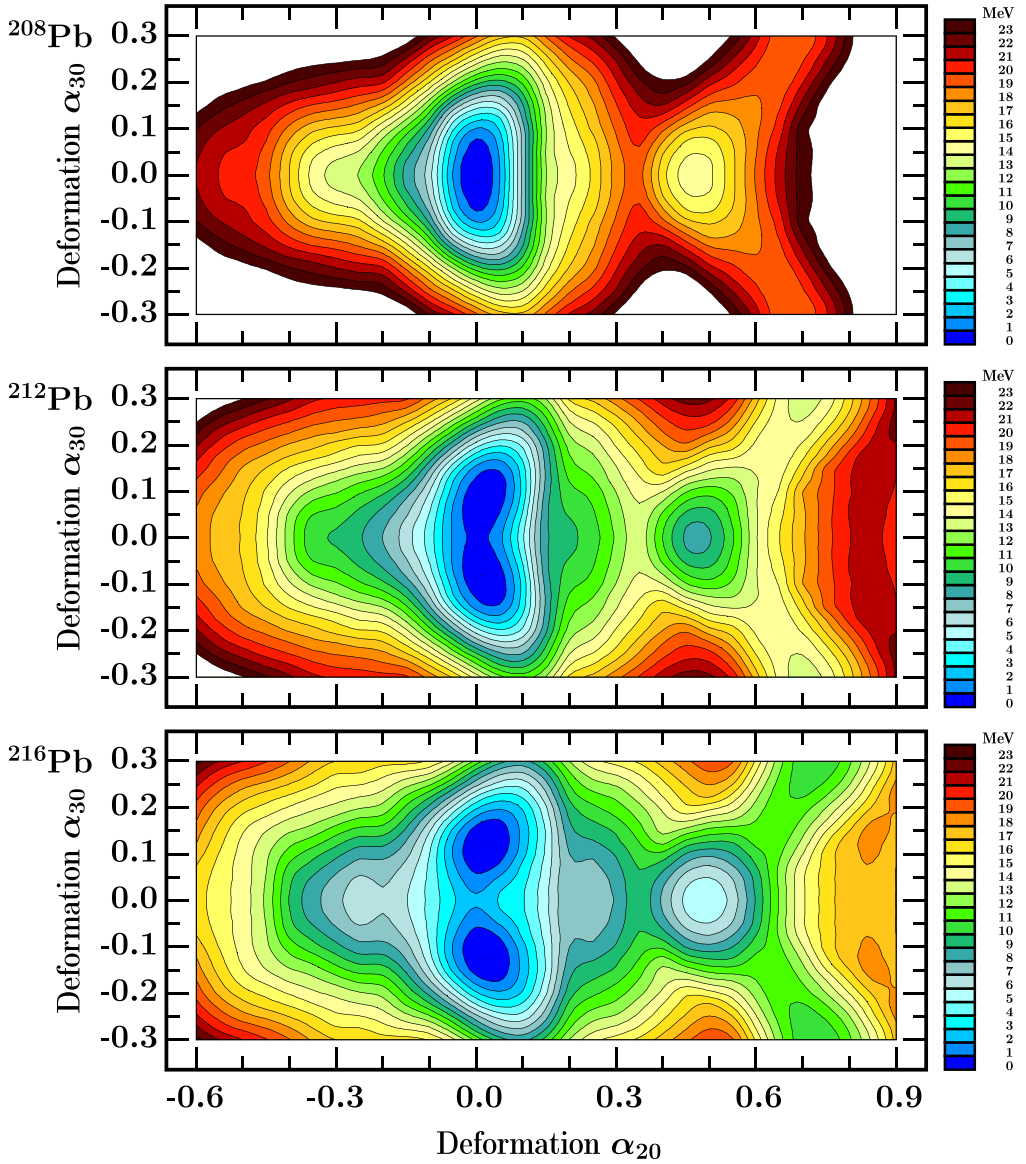

FIG. 5. Projections of the total nuclear energy on the $(\alpha_{30}, \alpha_{20})$ plane minimized at each point over triaxial quadrupole α_{22} and axial hexadecapole α_{40} deformations for ^{208,212,216}Pb nuclei resulting from our mean-field modeling. Comparison shows a buildup of octupole susceptibility at $N = 130$ (for ^{212}Pb), down to a strong octupole deformed minimum separated by the potential barrier of over 2 MeV height at $N = 134$ (for ^{216}Pb). The present collection of maps illustrating the pear-shape projections turns out to be characteristic for other octupole $\alpha_{3\mu\neq 0}$ components in Pb nuclei, up to minor details.

minima combined with the low-lying octupole $K^\pi = 2^-$ and $K^\pi = 3^-$ vibrations and the associated octupole bands. On the other hand, T_d and D_{3h} exotic-symmetry bands set in and compete with the others. All these structures and their evolution can be followed and identified with the present day nuclear structure instrumentation, and the rest of this article will be devoted to presenting the suggested modeling and identification methods.

It will be instructive to begin the discussion by enumerating the unique nuclear structure elements in the Pb nuclei, in order to treat those as a reference while proceeding to the presentation of the particularities of this evolution towards extended sectors of the mass table.

To start, let us emphasize a strongly appealing nuclear structure mechanism: The shape evolution in question is dominated by shell energies which originate from one kind of nucleons, the neutrons, whereas proton contributions are constrained by the presence of the dominating $Z = 82$ closure. Therefore, to a leading order, we are dealing here with the result of octupole repulsion between characteristic high-ℓ (high-j) neutron orbitals, $2g_{9/2}$ and $1j_{15/2}$ as discussed in the text surrounding Figs. 1–4.

Second, the results presented in the preceding section carry an important message about clearly visible spherical-shape instabilities of the majority of Pb nuclei, many of which are traditionally considered "just spherical" or "nearly spherical."

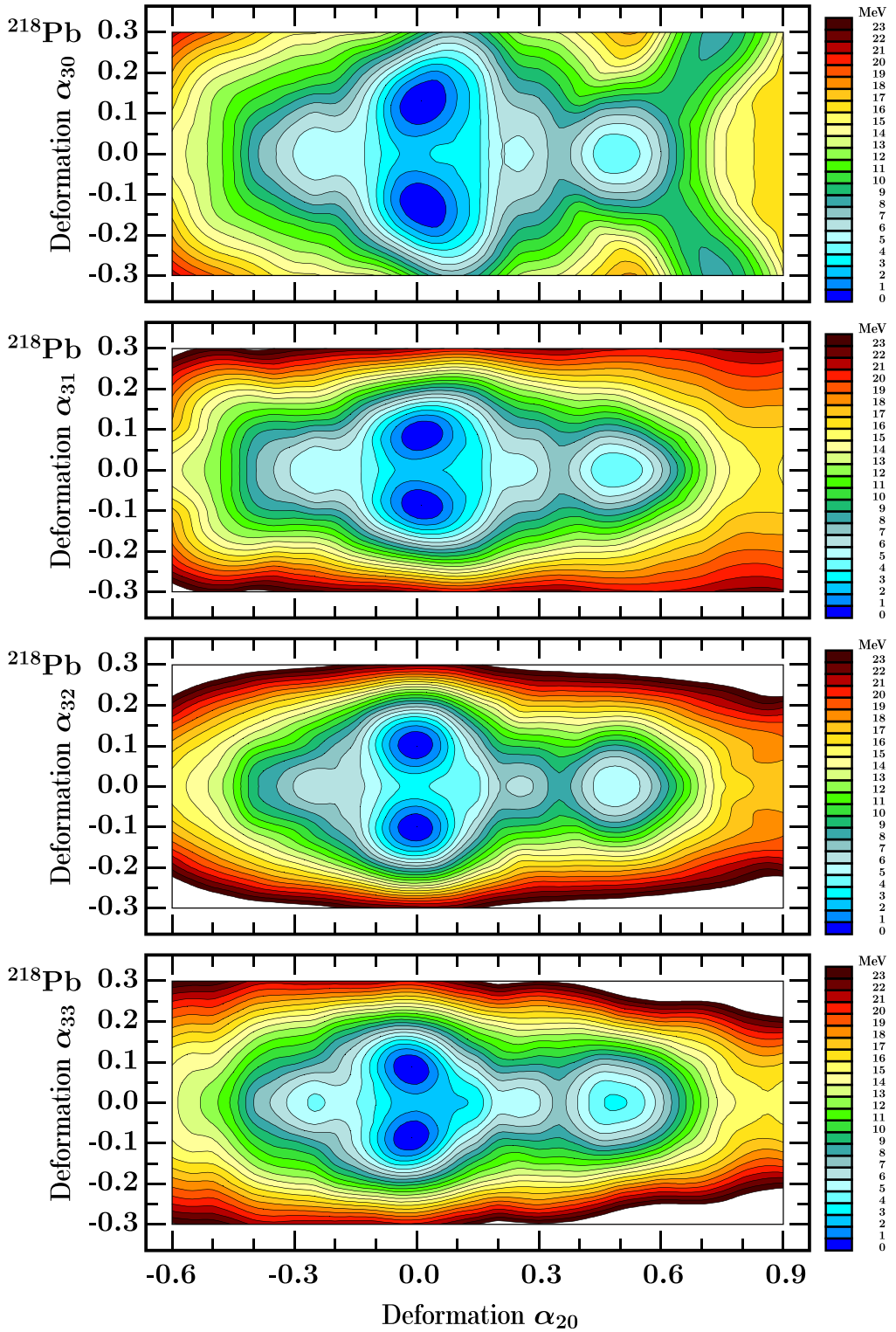

FIG. 6. Results structurally similar to those in Fig. 5, here comparing potential energy projections for the octupole "supermagic" number $N = 136$ (see Figs. 1–4), with all four μ projections, $\alpha_{3\mu} \leftrightarrow \alpha_{30}, \alpha_{31}, \alpha_{32}, \alpha_{33}$, for the ^{218}Pb$_{136}$ nucleus. Given the fact that combining $Z = 82$, having relatively weak octupole proton effects, with $N = 136$ accumulates the strongest neutron octupole effects, we should consider the present comparison as representing the purest manifestations of the $N = 136$ "supermagic" gap.

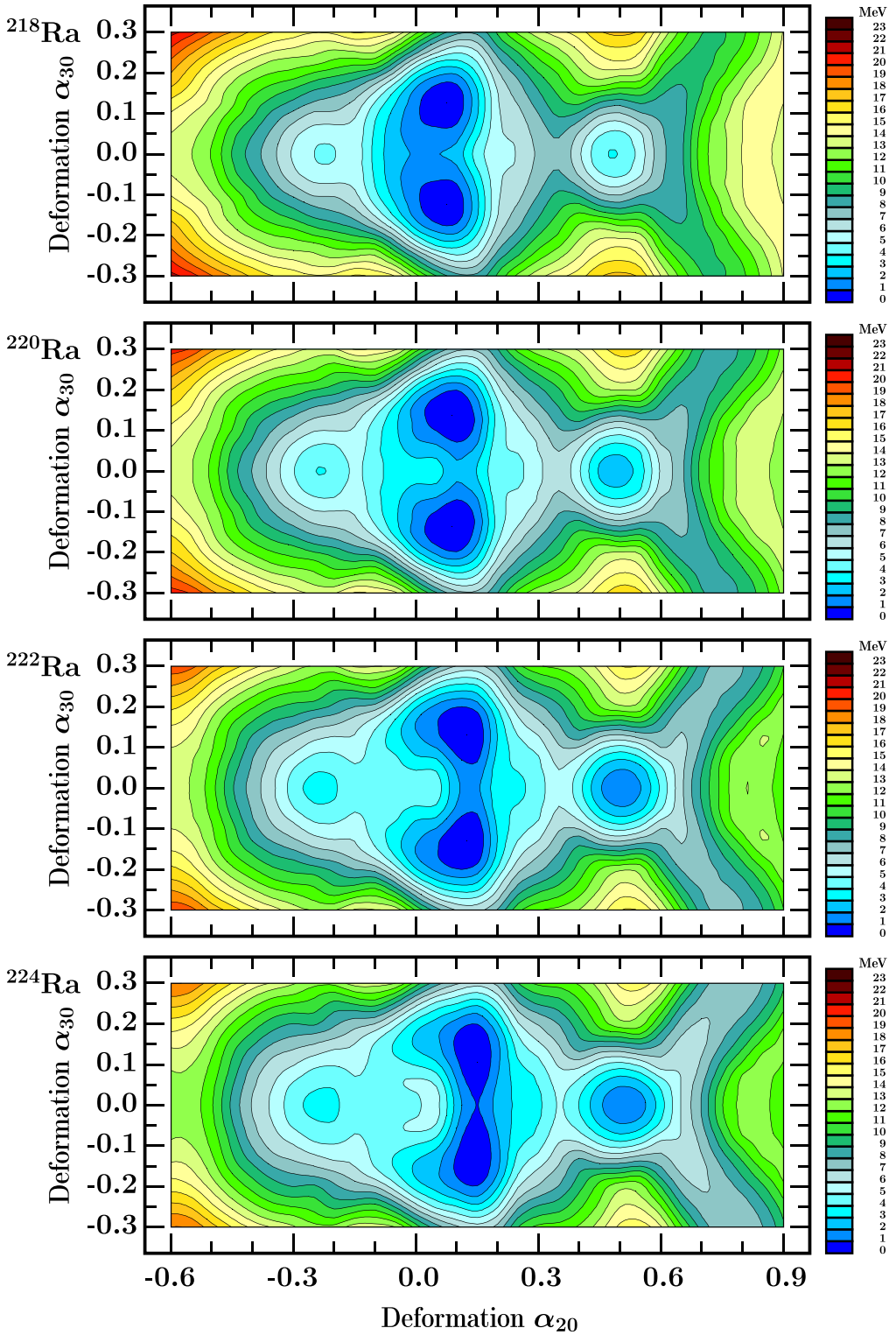

FIG. 7. Map selection focusing on the differences in terms of the pear-shape octupole evolution at the $Z = 82$ proton configuration (preceding figures) and larger proton numbers, here with radium, $Z = 88$, chosen as an example. We wish to emphasize that, in contrast to the tendency visible from Figs. 5 and 6 for the $Z = 82$ case, there is a buildup of nonvanishing quadrupole deformation on top of the $\alpha_{30} \approx \pm 0.15$ octupole doublets. The quadrupole components of equilibrium deformations evolve from $\alpha_{20} \approx 0$ to $\alpha_{20} \approx 0.15$ for increasing neutron number $N = 126, 128, 130, \ldots, 136$. The underlying symmetry corresponds to the point group $C_{\infty v}$. The calculated equilibrium values are $\alpha_{20}^{\text{th}} = 0.075$, 0.125, and 0.150 for ^{218,222,224}Ra compared with experimental ones from Ref. [38]: $\alpha_{20}^{\text{exp}} = 0.0910^{+49}_{-39}$, 0.1915(76), and 0.179^{+11}_{-8}, the closeness illustrating the predictive power of the universal parametrization.

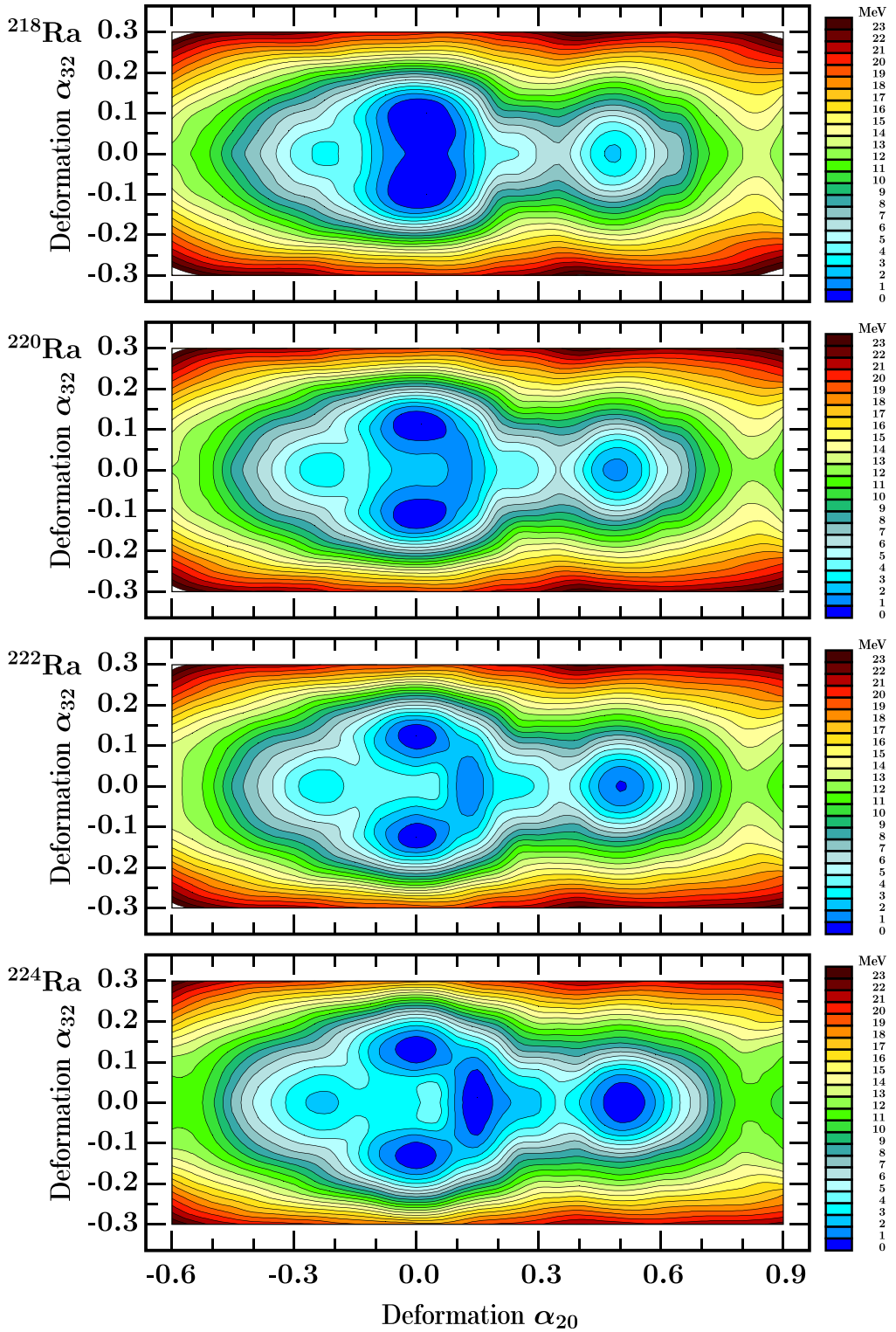

FIG. 8. Map selection focusing on the illustration of the systematic differences between the shape evolution for α_{30}, Fig. 7, and here, α_{32}. Observe the buildup of a ground-state quadrupole deformed minimum in parallel with the pronounced $\alpha_{32} \approx \pm 0.15$ tetrahedral minima. A flat energy zone around $\alpha_{20} \approx 0$ developing in ^{218}Ra$_{130}$ ends up with the $\alpha_{20} \approx 0.15$ ground-state minimum in ^{224}Ra$_{136}$. Notice a parallel buildup of the well-pronounced tetrahedral minima at $\alpha_{32} \approx \pm 0.15$ with $\alpha_{20} = 0$. They are predicted to generate rotational bands with vanishing collective $E2$ and $E1$ transitions [9].

However, as can be seen from Fig. 5, already at the neutron number $N = 130$ we predict a nonspherical pear-shape equilibrium deformation, a tendency which accelerates quickly with increasing N.

Third, there is yet another specificity of the discussed shape evolution: the pear-shape octupole susceptibility, along with a buildup of significant instability, takes place with no competition from the quadrupole components. The same applies to other octupole shape components. In other words, the equilibrium deformations in question are determined by the lowest order shape multipolarities ($\alpha_{20} = 0, \alpha_{3\mu} \neq 0$). It then follows that the corresponding experimental studies of the excitation spectra in the discussed nuclei primarily provide information about *octupole shapes as the leading order mechanism*, the quadrupole one playing, unusually, a secondary role.

The fourth observation in the series is noticing that the pear-shape effects are accompanied by comparably strong effects generated by all three $\alpha_{3\mu\neq 0}$ components; see Fig. 6. Moreover, the α_{32} octupole-tetrahedral shell effects are manifestly stronger than the ones related to the pear-shape configurations for reasons resulting from the properties of the irreducible representations of the T_d^D group introduced in Sec. II B. This unique structural feature may turn out to be of primordial importance for the present discussion, since, if the tetrahedral structures dominate, they induce the presence of a new class of isomers (discussed in detail in the article discovering the presence of these symmetries in subatomic physics, Ref. [9]), opening new frontiers in terms of experimental perspectives.

The symmetry point groups corresponding to a superposition of nonzero axial quadrupole shape components, $\alpha_{20} \neq 0$, with the nonzero octupole components are formally the same in three out of the four cases. Indeed, both ($\alpha_{20} = 0$, $\alpha_{30} \neq 0$) and ($\alpha_{20} \neq 0, \alpha_{30} \neq 0$) lead to $C_{\infty v}$ point group symmetry. Analogously, comparing the formal symmetries induced by ($\alpha_{20} = 0$, $\alpha_{31} \neq 0$) and the combination ($\alpha_{20} \neq 0, \alpha_{31} \neq 0$) leads to a common result, the point group C_{2v}. In contrast, whereas the deformation $\alpha_{32} \neq 0$ represents the tetrahedral symmetry group mentioned earlier, superposing ($\alpha_{20} \neq 0, \alpha_{32} \neq 0$) leads to another point group, D_{2d}. Finally, both ($\alpha_{20} = 0, \alpha_{33} \neq 0$) and the combination ($\alpha_{20} \neq 0, \alpha_{33} \neq 0$) generate a common symmetry, D_{3h}, in both cases.

We arrive in this way at the notion of exotic symmetries which will be adopted in this project:

> *The octupole bands, a term implicitly referring to a pear-shape geometry, were studied for over a half a century and are considered a standard element in nuclear structure theory. In contrast the geometries behind the point group symmetries C_{2v}, T_d, D_{2d}, and D_{3h} are referred to as "exotic" in the present article.*

The differences between rotational band properties (see Sec. IV), generated by distinct symmetries just listed, as predicted by group representation theory, are very significant and can be used for the experimental identification of the symmetries in question. In particular, observation of the presence or absence of certain characteristic levels, alternatively of double or triple degeneracies of levels as band members, provides unique arguments in favor (or disfavor) of identification of symmetries. Therefore, instrumentation capable of detecting (possibly weak) electromagnetic signals will generally be sufficient, provided that such levels are populated/depopulated by electromagnetic transitions at all.

Exact tetrahedral symmetry leads to specific, unique exotic structures. Indeed, in the latter case both collective $E1$ and $E2$ transitions vanish [9], which can be seen as an important obstacle when trying to identify such symmetry via systems of γ detectors. Fortunately, such limitations do not apply for D_{2d} symmetry. The latter can be seen as the result of tetrahedral symmetry broken by a quadrupole one. This offers a fascinating possibility of studying, among others, a weak T_d-symmetry breaking by observing weak but nonvanishing electromagnetic $E2$ and/or $E1$ transitions.

We emphasize that the commonly discussed manifestations of the pear-shape octupole deformations take the form of the so-called octupole bands or parity-doublet bands, mechanisms accompanied by other measurable signals such as frequency staggering with increasing spin, correlations between the reduced transition probabilities, characteristic angular momentum alignment properties, and more; see the reviews in Refs. [7,8,36] and monographs in Refs. [35,37]. Those typical rotational octupole bands were predicted to correspond to equilibrium shapes with simultaneous non-null quadrupole and pear-shape contributions ($\alpha_{20} \neq 0, \alpha_{30} \neq 0$). One should expect that varying quadrupole components in the nuclear shape will influence the relations between the reduced transition probabilities, $B(E2)$ vs $B(E1)$ and $B(E3)$, thus facilitating identification.

However, it is equally natural to expect that alternative observable signals generated by the rotational motion, such as staggering or angular momentum alignment properties, will be significantly influenced by the presence of the quadrupole or other strong octupole effects. The corresponding analysis in terms of the Hartree-Fock-Bogolyubov cranking (HFBC) approach is in progress and the results will be published elsewhere.

B. Octupole $\alpha_{3\mu}$ exotic shapes in $Z > 82$ nuclei: Implied evolution of exotic symmetries

The purpose of the following discussion is to provide a synthetic description of the predicted evolution of shapes driven by the octupole $\alpha_{3\mu}$ deformation components and the associated exotic symmetry properties with varying proton and neutron numbers. In what follows, we have preselected a sector of the nuclear mass table covering the zone of newly predicted symmetry effects. Our selection of graphical illustrations is intended as a compromise between presenting all the new symmetries and their evolutions on the one hand, and the possibilities of populating such nuclei in experiments aiming at identifying the theoretically predicted structures on the other.

It follows from the results presented so far that the octupole effects of interest set in from $N = 132$ onwards, reaching their most pronounced manifestations at $N = 136$. In Figs. 7 and 8 we present sequences of total potential energy maps illustrating the evolution of the octupole deformations, α_{30} (the most studied in the literature in the past) and α_{32} (the

most pronounced in terms of the shell effects due to the underlying tetrahedral symmetry) in the $N = 130, 132, 134, 136$ isotopes. Among nuclei with $Z \in [84, 90]$ we select for this illustration the $_{88}$Ra nucleus, for which a relatively big amount of experimental information already exists in the literature, signifying that the production of the corresponding excited configurations in a laboratory should not lead to extreme technical or instrumental difficulties.

In reference to the octupole pear-shape evolution, our calculations predict a competition between the unstable octupole ground-state configurations and the superdeformed minima at $\alpha_{20} \approx 0.5$, as well as faint, oblate-shaped minima at $\alpha_{20} \approx -0.25$. Within this general pattern, the flat α_{30} octupole valley corresponding to $\alpha_{20} = 0$ for ^{214}Ra$_{126}$ gets even more elongated for ^{216}Ra$_{128}$ (none of them shown) and transforms next into a sequence of double-minimum structures in the $^{218–224}$Ra$_{130–136}$ nuclei, as shown in Fig. 7. We emphasize that the transition mentioned is accompanied by a steady increase in quadrupole equilibrium deformations, starting with $\alpha_{20} \approx 0.03$ in ^{218}Ra and ending with $\alpha_{20} \approx 0.15$ in ^{224}Ra.

In terms of predictions comparable to experiments, our calculations suggest that, while the octupole radiation $B(E3)$ strengths should be comparable among nuclei in the discussed sequence, the collective quadrupole transition strength should be gradually increasing. The evolution just described can be seen as characteristic for the whole sequence of Pb, Po, Rn, Ra, and Th nuclei as far as octupole pear-shape geometry is concerned and thus Fig. 7 can be seen as representative for all mentioned nuclei.

The corresponding symmetry point group characterizing the discussed shapes is known in group theory as $C_{\infty v}$. From the mathematical viewpoint, the latter symmetry remains formally the same no matter whether the quadrupole component vanishes or not.

Concerning the evolution of the α_{31} deformation properties represented by the maps similar to those in Fig. 7, in which α_{30} on the vertical axis is replaced by α_{31}, our calculations predict a full analogy in terms of the just described behavior, except for an increase in α_{20} component, its growth being slightly slower when the neutron number increases. Given the similarities between the α_{30} and α_{31} behavior, the latter evolution is not shown.

The symmetry behind the shape evolution in the latter case, guided by the octupole component α_{31}, is known in group theory as C_{2v}; it remains the same for both vanishing and nonvanishing α_{20}.

In contrast to the evolution pattern behind the results in Fig. 7, the symmetry evolution driven by α_{32} octupole deformations with increasing neutron number can, very interestingly, be considered qualitatively different; see Fig. 8. Indeed, the flat α_{32} octupole valley for $N = 126$ and 128 evolves into a double minimum in ^{218}Ra with a progressively increasing barrier separating the two minima, with N varying between 130 and 136; see Fig. 8. Yet the associated quadrupole deformation component remains constant: $\alpha_{20} = 0$. The symmetry behind the α_{32}-driven evolution corresponds to, in mathematical terms, the strict tetrahedral point-group T_d, imposing hindrance in terms of collective $E2$ and $E1$ transitions and predicted buildup of implied isomeric structures expected to manifest themselves also at increasing angular momenta.

And yet, along with the development of the tetrahedral minima of increasing separation strength, a valley parallel to the vertical (α_{32}) axis corresponding to a non zero quadrupole deformation ($\alpha_{20} \approx 0.25$) builds up, the onset being visible for ^{220}Ra, getting stronger for ^{222}Ra, and finally building up a ground-state minimum for ^{224}Ra, the evolution of which is visible in Fig. 8. The implied nuclear oscillatory motion combines simultaneously the $\alpha_{32} \neq 0$ and $\alpha_{20} \neq 0$ deformations. In this way a competing symmetry develops which is associated, in group theory language, with the D_{2d} point group. Correspondingly, in addition to the two axial-symmetry minima visible from Fig. 8 at $\alpha_{20} \approx 0.50$ (superdeformed) and at $\alpha_{20} \approx -0.25$ (oblate shape) the tetrahedral symmetry band enters the competition possibly accompanied by a rotational band built on a D_{2d}-symmetry configuration.

C. Comparison of similarities and differences in $\alpha_{3\mu}$ effects at the universal magic number $N = 136$

As described in the preceding sections, the nuclear structure effects manifested as functions of the four octupole deformations show certain characteristic parallels, but also equally characteristic differences. In particular, we note similarities in terms of the shape evolution with the proton numbers between α_{30} and α_{31} on the one hand, and between α_{32} and α_{33} on the other.

For a graphical illustration, we have chosen to fix the neutron number at the octupole supermagic number $N = 136$ to emphasize the strongest shell effects produced by the neutrons and modify the proton number to be able to cover the comparison zone including Pb, Po, Rn, Ra, and Th nuclei. Strictly speaking, because of the graphical format's limitations in this section we are able to compare only the properties of the last four nuclei just mentioned; we profit from the fact that the analogous results for the Pb nuclei are presented in Sec. III A, where we introduced the general lines of discussion of this article.

1. Effects of α_{30} in Po, Ra, Rn, and Th: Symmetry $C_{\infty v}$

Referring to the results in Fig. 9, the pear-shape octupole "north-south" valleys align vertically at quadrupole deformation, increasing approximately from $\alpha_{20} = 0.10$ to 0.15, for $Z = 84$, 86, 88, and 90 nuclei, an evolution which can be seen as a parallel shift. The *flatness* of the bottom of the discussed valley implies that, from the experimental view point, *one should expect the $I^\pi = 1^-$ and 3^- lowest negative parity band members to be positioned close to or higher than the energies of the positive-parity band members, $I^\pi = 4^+$*. Indeed, the qualitative features of these particular aspects of the octupole-band related spectra are illustrated in Fig. 1.7 of Ref. [37]; see the surrounding comments and discussion in that reference.

From experimental results in Ref. [39] we find

$$^{226}\text{Th}: \; E_{I^\pi=1^-} = 230.4 \text{ keV}, \; E_{I^\pi=3^-} = 307.5 \text{ keV}, \quad (17)$$

$$\text{against } E_{I^\pi=4^+} = 226.4 \text{ keV}, \quad (18)$$

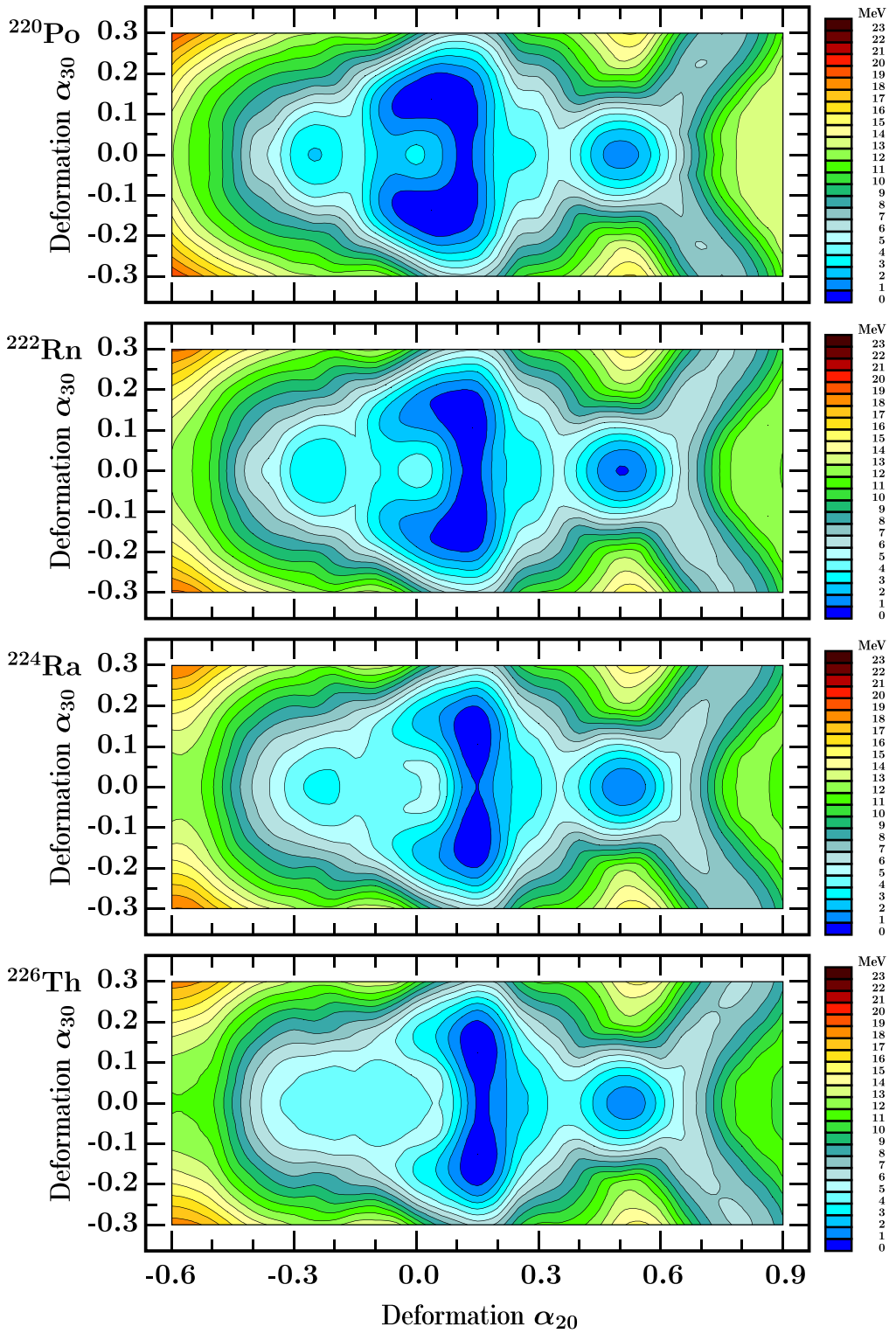

FIG. 9. Focus on the octupole supermagic number $N = 136$. We follow the quadrupole shape increase at the pear-shape deformation $\alpha_{30} \approx \pm 0.15$ from $\alpha_{20} \approx 0$ at $^{220}_{84}$Po up to $\alpha_{20} \approx 0.15$ at $^{226}_{90}$Th. The corresponding point group symmetry is $C_{\infty v}$. The experimental quadrupole equilibrium values known for ^{222}Rn, ^{224}Ra, and ^{226}Th, Ref. [38], $\alpha_{20}^{\rm exp} = 0.1417(45)$, 0.1790^{+11}_{-8}, and 0.2299(19), should be compared to the calculated ones, $\alpha_{20}^{\rm th} = 0.13$, 0.15, and 0.16, respectively.

i.e., 3^- higher than 4^+, together with

$$^{224}\mathrm{Ra}: \; E_{I^\pi=1^-} = 216.0 \text{ keV}, \; E_{I^\pi=3^-} = 290.4 \text{ keV}, \quad (19)$$

$$\text{against } E_{I^\pi=4^+} = 250.8 \text{ keV}, \quad (20)$$

i.e., similar inequality as in the preceding case, and finally

$$^{222}\mathrm{Rn}: \; E_{I^\pi=1^-} = 600.7 \text{ keV}, \; E_{I^\pi=3^-} = 635.5 \text{ keV}, \quad (21)$$

$$\text{against } E_{I^\pi=4^+} = 448.4 \text{ keV}. \quad (22)$$

There are no experimental results for ^{220}Po available.

This comparison shows a good semiquantitative correspondence with the expectations based on general considerations summarized in Ref. [37], which can be seen as a very encouraging argument in favor of the predictive capacities of the modeling employed.

The just-described scenario related to the α_{30} evolution should be considered standard, "nonexotic" according to our nomenclature. Similar properties have been discussed in many nuclei in the literature, and the present discussion serves to provide a reference point allowing to define the systematic similarities and possibly systematic differences in the discussion of the exotic symmetry effects that follows.

2. *Effects of α_{31} in Po, Ra, Rn, and Th: Symmetry C_{2v}*

The following comparison is analogous to the previous one with α_{30} dependence of the potential energy surfaces replaced by the first nonaxial one, α_{31}. We will refer to the results in Fig. 10 showing at first glance a full analogy manifested by the presence of the "north-south" valleys which, up to certain details, repeat the pattern of the parallel shift of the α_{20} position, varying from about 0.10 to 0.15, with increasing proton number, as discussed in the previous section. On top of this systematic similarity we also notice a systematic difference in that the valleys are slightly broader and shorter in terms of the coordinates α_{31} vs α_{20}.

To a leading order one may expect that corresponding vibration energies should be slightly higher compared to those from the previous section, given the fact that the stiffness coefficients of the potential valleys are predicted to be smaller here. Strictly speaking, to confirm the last affirmation one would need to solve the Schrödinger equation with the microscopically calculated mass tensor, employing the new concepts of nuclear adiabaticity, Ref. [40]. Corresponding calculations are in progress and the results will be presented elsewhere.

3. *Effects of α_{32} in Po, Ra, Rn, and Th: Symmetries T_d and D_{2d}*

We continue with our step-by-step discussion of the systematic analogies and differences within the potential energy structures generated by the octupole shape degrees of freedom, here the second nonaxial octupole, and also tetrahedral-symmetry shape, α_{32}; see Fig. 11.

The new mechanism predicted is the presence of the tetrahedral symmetry configurations manifested by the double minima at $\alpha_{32} \approx \pm 0.15$ combined with $\alpha_{20} = 0$. It is the latter feature, the vanishing of the quadrupole shape component, together with the presence of the potential barriers which surround the discussed minima of approximately 1–2 MeV heights, which lead us to the prediction of a presence of possibly the purest realization of the tetrahedral (T_d) symmetry minima in the discussed nuclei. The interested reader may consult Ref. [9] for the description of the experimental procedure of searching for the identification of such structures and their appearances (to our knowledge this is the first and the only identification case published so far).

In contrast, the analogous systematic mechanism seen in the present case is the appearance, with increasing Z, of axial-symmetric quadrupole minima at $\alpha_{20} \approx 0.15$. Such minima in the α_{32} vs α_{20} coordinate plane are expected to generate two types of oscillations, which to a leading order should parallel to the well-known quadrupole β and γ oscillations manifested experimentally via the "second" $I^\pi = 0^+$ and $I^\pi = 2^+$ vibrational states. Experimentally, the oscillations in the α_{32} direction are expected to generate $K^\pi = 2^-$ (negative parity) vibrational bandheads and the associated rotational bands, analogous to the γ bands.

Finally let us remark in passing that all the structures discussed so far are predicted to be in competition with the axial-symmetric superdeformed minima at $\alpha_{20} \approx 0.5$, at low excitation energies comparable to the ground-state ones within some hundreds of keV difference.

4. *Effects of α_{33} in Po, Ra, Rn, and Th: Symmetry D_{3h}*

We complete our step-by-step presentation of nuclear potential energy properties, here generated by the third and the last family of nonaxial octupole shapes, spanned by the α_{33} multipole parameter, inducing the presence of the threefold symmetry axis (120° discrete rotation symmetry axis implying the D_{3h} point group). As before we observe (see Fig. 12) a systematic tendency of increase in the axial-symmetry quadrupole-deformed ground-state minima, whereas the double α_{33} minima at $\alpha_{20} = 0$ get less and less pronounced with the proton number increasing, $Z = 84$, 86, 88, and 90.

According to results in Fig. 12, D_{3h} symmetry appears in the discussed four representative nuclei in two qualitatively different forms, which we refer to as static and dynamic ones.

Strictly speaking we might expect that the static D_{3h} configurations must be characterized by double minima, each centered at some positive and negative nonvanishing value, $\alpha_{33} \neq 0$, and at the same time accompanied by sufficiently high surrounding potential barriers. The term "sufficiently high" can be considered vague, but in semiquantitative terms, since the energies of the corresponding vibrational states are expected at the level of several hundreds of keV, barriers well in excess of 1 MeV, e.g., 1.5 MeV or more, most likely provide a sufficient stability.

On the theory side much more precise information can be reached by solving the Schrödinger equation of the collective model of Bohr as in the case of the approach of Ref. [40] cited earlier in a similar context. The corresponding project is being followed independently of the present one, and the results will be published in a forthcoming article.

Whereas the total energy maps suggest favorable conditions for the D_{3h} configurations in ^{222}Rn and ^{220}Po in their

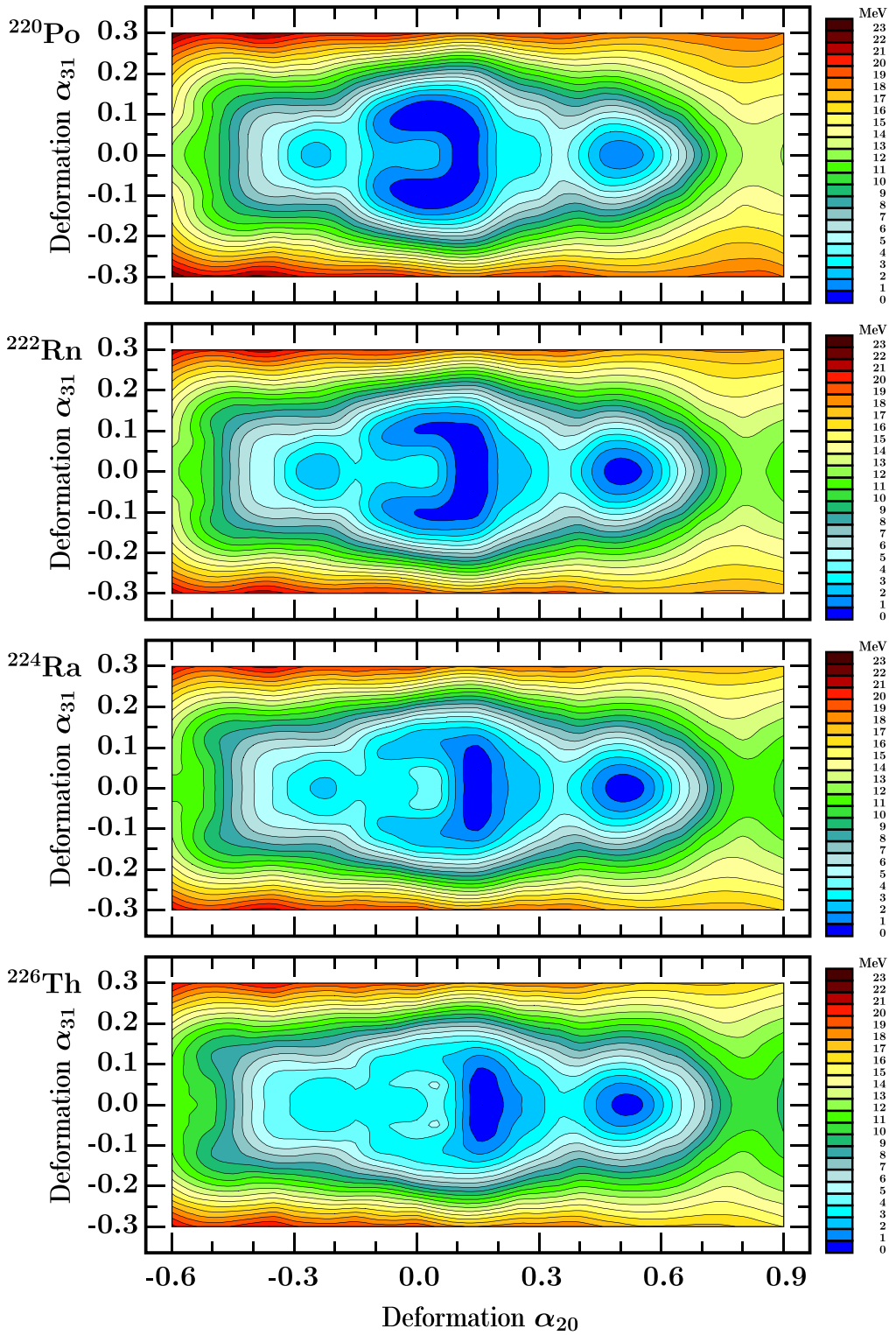

FIG. 10. Focus on the octupole supermagic number $N = 136$. Here we wish to stress a semiquantitative correspondence and similarities between α_{30} deformation evolution, as shown in Fig. 9, and α_{31} for the same choice of the nuclei compared. The ground-state configuration point group symmetry is C_{2v}.

static variants, so that experiments aiming at their identifications may be tempting, the conditions in the remaining two nuclei in Fig. 12 seem much less favorable. However, according to mathematical arguments based on group theory, one should expect the presence of two forms of oscillatory motion, one in terms of α_{20} (quadrupole vibrations) and one in terms of α_{33}, here referred to as D_{3h} oscillations or the dynamical D_{3h} effect. In the latter case we should expect existence of

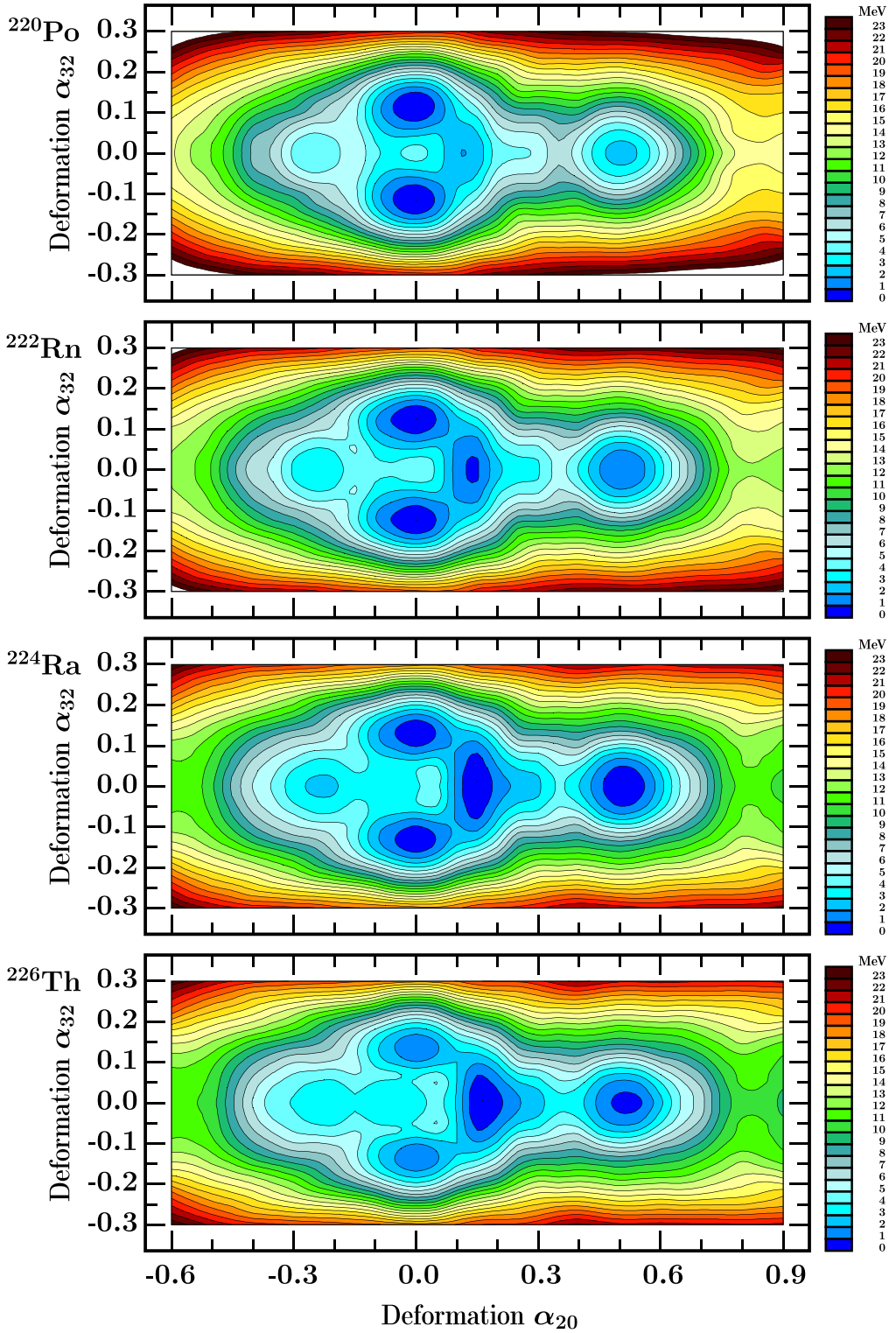

FIG. 11. Focus on the octupole supermagic number $N = 136$, here emphasizing the basic differences between the shape evolution induced by α_{32} as compared to the α_{30} and α_{31} cases illustrated in Figs. 9 and 10, respectively. The novelty, compared to the previous cases, consists in the fact that the tetrahedral double minimum at $\alpha_{32} \approx \pm 0.15$ and $\alpha_{20} \approx 0$ stays in place when the proton number increases from $Z = 84$, i.e., ^{220}Po, up to $Z = 90$, i.e., ^{226}Th, whereas in parallel an axial-quadrupole symmetry ground-state minimum builds up at $\alpha_{20} \approx 0.15$. In the discussed case we deal with two coexisting symmetries, one associated with the static T_d double minimum, the other associated with the ground-state α_{32} oscillations at $\alpha_{20} \approx 0.15$, leading to dynamic realization of D_{2d}.

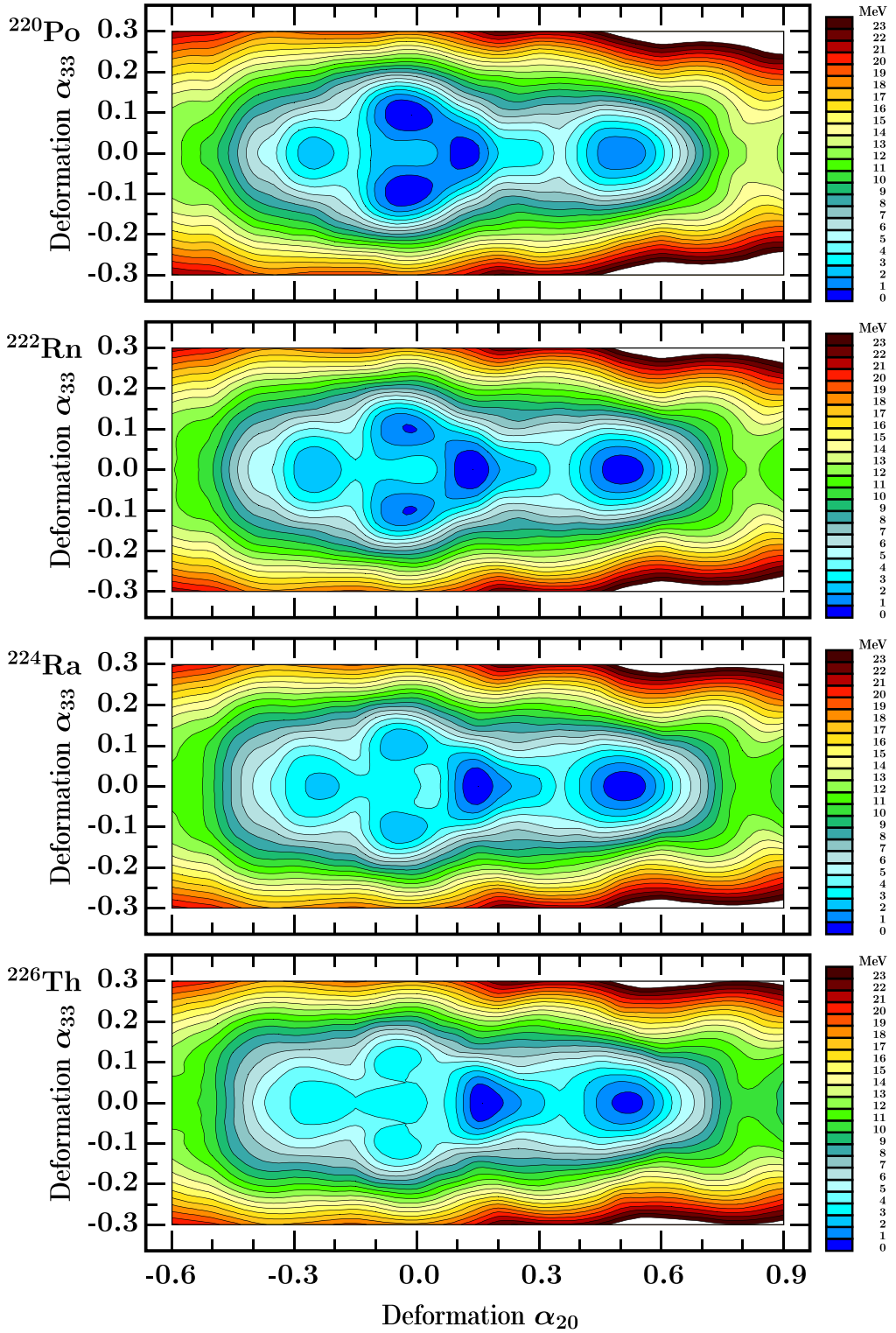

FIG. 12. Illustration analogous to the preceding one, here focusing on the octupole deformation α_{33} in place of α_{32} in Fig. 11. In the present case, the double α_{33} minima, combined with $\alpha_{20} \approx 0$ characteristic of the D_{3h}-symmetry point group, are less pronounced, whereas the axial symmetry quadrupole ground-state minimum with $\alpha_{20} \approx 0.15$ sets in firmly beginning with $N = 132$.

the $K^\pi = 3^-$ vibrational states which may become bandheads of the corresponding rotational bands, possibly carrying the signs of their underlying symmetry.

More precise mathematical conditions built on group-representation theory will be employed to construct the experimental identification criteria in Sec. IV.

IV. IDENTIFICATION CRITERIA OF EXOTIC SYMMETRIES VIA COLLECTIVE ROTATION

In the preceding sections we discussed a number of mechanisms which may generate the presence of exotic shape symmetries, in particular in the heavy lead isotopes but also in numerous heavier nuclei in their neighborhood. Among those nuclei, many have already been populated in various nuclear reactions and published experimental evidence suggests that specific experiments aiming at identification of the predicted exotic-symmetry structures are possible. Recall that we apply the name "exotic symmetry" by definition neither to quadrupole- nor to axial-symmetry octupole-deformed shapes.

Results presented so far illustrate the link between these symmetries and the shell effect caused by repulsion between the neutron $2g_{9/2}$ and $1j_{15/2}$ orbitals, the proton shell structures playing a relatively minor role, if any, then by slightly destabilizing the exotic symmetry structures. The repulsion between the two neutron orbitals was attributed in the literature to the octupole-octupole residual interactions or alternatively the mean-field octupole deformations [34]. This generates shell effects, which in turn cause the octupole shape susceptibility in the form of the flatness of the potential energy landscapes, alternatively in the form of the well-developed static minima. In majority of the discussed nuclei this mechanism leads to the $\alpha_{3\mu}$ deformation effects *for all four octupole degrees of freedom simultaneously,* as illustrated in the preceding section.

A. Evolution of the octupole magic-gap structure with rotational frequency

In the following sections we will study the specific properties of rotational bands generated by exotic symmetries in nuclei of interest with the idea of using their unique features for identification of their presence experimentally. Before proceeding, it will be instructive to test the evolution of the exotic shell structures with increasing spin or, alternatively, increasing rotational (cranking) frequency. Indeed, in order to be able to employ the underlying theoretical methods focusing on the rotational properties, e.g., in experimental proposal writing, it will be instructive to verify whether the corresponding shell effects resist the impact of the increasing rotational frequency.

To this end we are going to employ a 3D cranking approach by solving the corresponding mean-field cranking problem with the Hamiltonian

$$\hat{H}_{WS} \quad \rightarrow \quad \hat{H}^{\vec{\omega}}_{WS} = \hat{H}_{WS} - \vec{\omega} \cdot \hat{\jmath}, \tag{23}$$

where $\hat{H}_{WS}$ is given by Eq. (6) whereas $\vec{\omega} \equiv \{\omega_x, \omega_y, \omega_z\}$ and $\hat{\jmath}$ denotes the nucleonic angular momentum operator.

We have verified that increasing the rotational frequency induces a gradual closing up of the $N = 136$ magic gap, but at the same time modifying the directions of the cranking frequency vector with respect to the octupole deformed nucleus does not influence the degree of this variation in any dramatic manner. It thus turns out that it will be sufficient to illustrate the whole mechanism with the help of simplified pictures of such changes by selecting one cranking axis as representative.

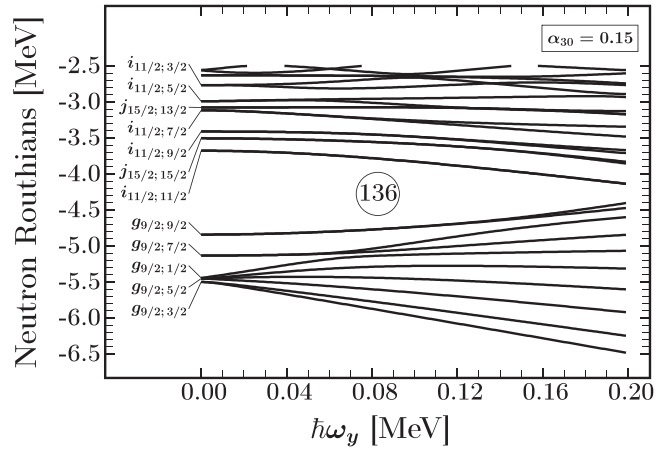

FIG. 13. Single particle neutron Routhians at pear-shape octupole deformation $\alpha_{30} = 0.15$ representative of potential energy minima predicted in heavy lead isotopes, as well as in several heavier nuclei. The gap opening at $\hbar\omega_y = 0$ is about 1.5 MeV and decreases as expected towards $\hbar\omega_y = 0.20$ MeV, the frequency at which the single-particle Routhian distribution becomes approximately uniform.

Figures 13–16 show four diagrams analogous to those in Figs. 1–4, with the single-particle energies replaced here by the single-particle Routhians corresponding to the $\mathcal{O}_y$-axis cranking as a representative illustration of the shell-gap evolution with nuclear cranking frequency, thus with the spin. Calculations indicate that the total (proton and neutron) angular momentum at the maximum frequency shown are of the order of $20\hbar$, an estimate representative of the nuclei in the mass zone discussed in this article. In what follows we will be interested in the rotational band structures corresponding to frequency intervals below the high-j alignment area and possibly a back-bending, which translates in terms of angular momentum into an interval of the order of a dozen $\hbar$.

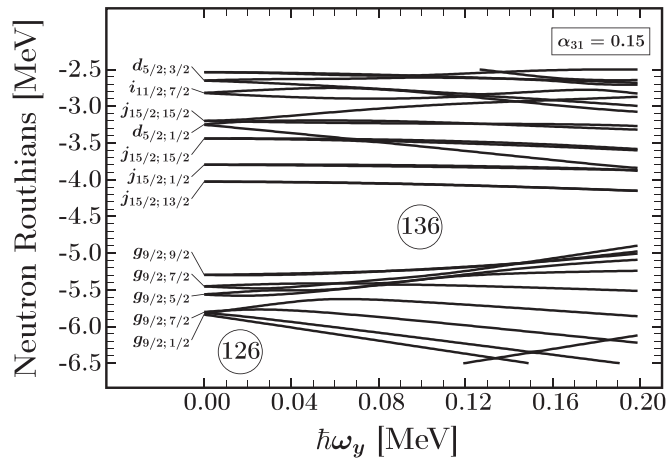

FIG. 14. Similar to the preceding figure, but for the $\alpha_{31} = 0.15$ octupole deformation. The α_{31} octupole gap at $N = 136$ and $\hbar\omega_y = 0$ is of the order of 1.5 MeV, slightly more than in the previous case, but the $N = 136$ gap manifests the highest stability against the cranking effect down to maximum $\hbar\omega_y = 0.2$ MeV considered here.

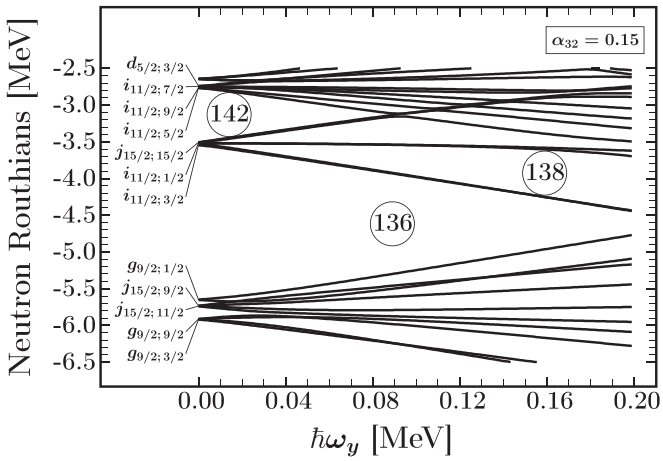

FIG. 15. Similar to the preceding figures, here for single-particle Routhians at deformation $\alpha_{32} = 0.15$ representing tetrahedral symmetry minima in many nuclei in the studied mass region. The low level density area including $N = 136$ and $N = 142$ gaps at $\hbar\omega_y = 0$ extends to almost 3 MeV and decreases to about 2 MeV at the maximum frequency illustrated, manifesting the strongest resistance against rotation.

Cranking calculations show, as expected, that the strongest shell effects around $N = 136$ correspond to the α_{32} tetrahedral symmetry case, Fig. 15, with the dominating shell gap closing at $\hbar\omega_y \approx 0.30$ MeV. A smaller $N = 136$ gap at α_{31} deformation, the C_{2v}-symmetry case, persists in the similar cranking frequency range; see Fig. 14. The pear-shape symmetry shell effects as function of the rotational frequency are clearly visible in Fig. 13, the main gap closing at $\hbar\omega_y \approx 0.25$ MeV. Finally, the case of α_{33} shell effects and the underlying geometry with the threefold symmetry axis is illustrated in Fig. 16, showing the least pronounced gaps. The shell effects are manifested mainly by the visibly low level density zones, which

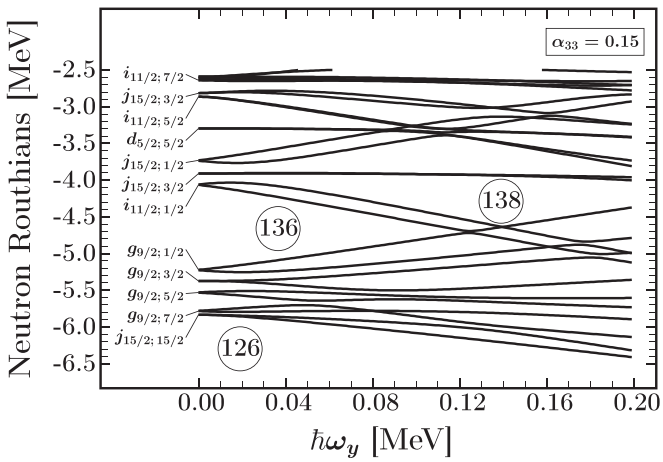

FIG. 16. Similar to the preceding cases, here for α_{33} octupole deformation representing a D_{3h} symmetry in potential energy minima in many nuclei in the discussed mass region. The octupole shell effect at $\hbar\omega_y = 0$ can be considered as the weakest in comparison to other cases and essentially takes the form of relatively low level density at $N = 136, 138$.

decrease with increasing frequency filling in the energy interval with the single-particle Routhians in an approximately uniform manner at $\hbar\omega_y \approx 0.15$ MeV.

We conclude that the mean-field cranking estimates modeling the mechanism of vanishing $N = 136$ octupole shell effects with increasing collective rotation clearly suggest a survival of such effects within, on average, at least the angular momentum zone within a dozen $\hbar$. This provides one more motivation to examine the rotational band properties as predicted by group representation theory at least within the discussed interval, which will be our following subject.

B. Rotational band properties in the presence of T_d octupole symmetry, deduced by employing point group theory

It will be instructive to begin our presentation of rotational properties of nuclei obeying selected point group symmetries by recalling two, in a way opposite, view-points, which nonetheless will be demonstrated to be complementary. They both aim at describing the same physical objects and phenomena:

(i) Rotating nuclei are described as structureless quantum rotors with their Hamiltonians constructed out of nuclear total angular momentum operators, $\hat{I} = \{\hat{I}_x, \hat{I}_y, \hat{I}_z\}$, using well-known tensor-coupling algebra. The underling mathematical formalism applied in the discussed context can be found, e.g., in Refs. [41,42]. It allows constructing the rotor Hamiltonians invariant under any predefined point-group symmetry of interest.

(ii) Alternatively, rotating nuclei are described within a microscopic mean-field theory extended to include the external rotation, the latter allowing an introduction of the angular momentum of rotation in this case. The external rotation is usually treated by employing the well-known mean-field cranking and Hartree-Fock-Bogolyubov cranking (HFBC) methods.

Without going into formal details, we consider it instructive to remind the reader about certain principles of the two approaches in order to present unifying symmetry aspects between the two, thus strengthening the final argumentation about experimental identification issues.

1. Pointgroup symmetric structureless quantum rotors

The first of the two approaches has an advantage of relative simplicity as compared to the more microscopic case, allowing for a direct calculation of the energy spectra as well as the reduced electromagnetic transition probabilities. The approach adapted to the present discussion, from Refs. [41,42], is based on the rotor Hamiltonian

$$\hat{\mathcal{H}}_{\rm Rot} = \frac{\hat{I}_x^2}{2\mathcal{J}_x} + \frac{\hat{I}_y^2}{2\mathcal{J}_y} + \frac{\hat{I}_z^2}{2\mathcal{J}_z} + \hat{h}(\{p\}; \hat{I}_x, \hat{I}_y, \hat{I}_z), \qquad (24)$$

in which the first term represents the "traditional" triaxial rotor with the moment of inertia parameters $\mathcal{J}_x$, $\mathcal{J}_y$, and $\mathcal{J}_z$, and the second term allows modeling point group symmetries with the help of adjustable parameters denoted $\{p\}$. It is composed

of the spherical-tensor operators involving the powers of angular momentum components higher than 2 and constructed using the Clebsch-Gordan coupling rules. The algorithm is fully analogous to the one applied in molecular physics, e.g., Refs. [43,44]. This formalism allows us to extend the context of collective excitations to include, in full analogy with the molecular physics applications, also the vibrations and the rotation-vibration coupling (see Ref. [42]):

$$\hat{\mathcal{H}}_{\rm Rot} \rightarrow \hat{\mathcal{H}}_{\rm Rot} + \hat{\mathcal{H}}_{\rm Vib} + \hat{\mathcal{H}}_{\rm VibRot}. \tag{25}$$

In the following we limit our interest to collective nuclear rotation and thus orientation of the rotor relative to a chosen Cartesian reference frame, the latter described with the help of Euler angles. The solutions allowing us to represent the probability of nuclear orientation in space and other collective properties can be obtained by a diagonalization method, as usual employing Wigner functions as a basis. The corresponding transformation properties of the solutions of the problem are conveniently written down with the help of the orthogonal group in three dimensions,

$$\mathrm{O}(3) = C_i \times \mathrm{SO}(3), \tag{26}$$

and its irreducible representations play a central role in what follows. Here C_i denotes the inversion group and SO(3) the (special orthogonal) rotation group, according to standard definitions and notation.

Information about point group symmetries of nuclear shapes and their impact on the properties of the nuclear rotational bands on the microscopic-structure level will be deduced by employing the mean-field theory with the cranking approximation, and will be addressed next.

2. *Projected mean-field theory: Link with Point groups*

In contrast to the structureless rotor picture introduced so far, the mean field theories in their various realizations address the solution of the nuclear motion in the language of the many-body problem written down, within a two-body interaction scheme, beginning with the Hamiltonian

$$\hat{\mathcal{H}}_{2-\rm Body} = \sum_{i_1 i_2} t_{i_1 i_2} \hat{c}^+_{i_1} \hat{c}_{i_2} + \frac{1}{2} \sum_{i_1 i_2 i_3 i_4} v_{i_1 i_2 i_3 i_4} \hat{c}^+_{i_1} \hat{c}^+_{i_2} \hat{c}_{i_4} \hat{c}_{i_3}, \tag{27}$$

in which the symbols t and v represent the kinetic energy and the two-body interaction terms, respectively, whereas $\hat{c}^+$ and $\hat{c}$ represent single-nucleon creation and annihilation operators. The mean-field ansatz is usually introduced with the help of the totally antisymmetric product states $\langle\Phi'|$ and $|\Phi\rangle$, allowing us to introduce the language of densities and the variational principle.

Geometrical symmetries enter the self-consistent mean field approach via external constraints taking the form of extra conditions imposed, e.g., on the expected values of the multipole moment operators

$$\langle\Phi|\hat{Q}_{\lambda\mu}|\Phi\rangle = Q_{\lambda\mu} \leftrightarrow \alpha_{\lambda\mu}, \tag{28}$$

where $Q_{\lambda\mu}$ are physicist-defined numbers, often chosen to correspond to the nuclear shape deformations introduced in Eq. (1); for instance, by specifying a series of values like $\alpha_{32} = 0.15, 0.20, 0.25\ldots$, we may calculate the nuclear energies according to the HFBC approach for increasing static tetrahedral deformations.

With or without constraints, the deformed mean fields lead to breaking of the original symmetries possibly carried by two-body interactions in Eq. (27) so that the quantum numbers characterizing the system in a laboratory reference frame such as the nuclear angular momentum I and parity π (or proton and neutron particle numbers in the case of Hartree-Fock-Bogolyubov approaches) need to be recovered using projection techniques. This is done with the help of the projection relations

$$\left|\Psi^{I\pm}_{M\kappa}\right\rangle = \sum_K g^{I\pm}_{K,\kappa} \hat{P}^I_{MK} \hat{P}^{\pm} |\Phi\rangle, \tag{29}$$

in which $\hat{P}^I_{MK}$ and $\hat{P}^{\pm}$ are angular momentum and parity projectors respectively, and where expansion coefficients, $g^{I\pm}_{K,\kappa}$, are obtained by solving the generalized eigenvalue problem within the formalism of Hill-Wheeler equations; see Ref. [11] for details.

Needless to say, describing the details of these procedures (which are standard today) bypasses the scope of the present article, but the interested reader may consult textbooks and review articles, such as Refs. [45–47] and references therein.

Let us open the principal subject of the discussion by presenting the results of the microscopic Hartree-Fock-Bogolyubov cranking calculations with the spin and parity projections, for one of the nuclei of primary interest in this article, $^{226}_{90}\mathrm{Th}_{136}$, corresponding to the "universal octupole magic number" $N = 136$ at which the tetrahedral-symmetry shell effects are the strongest. Results presented in Fig. 17 correspond to the lowest E_I vs I energy sequence obtained from the constrained, spin and parity projected HFBC calculations, with the Q_{32} moment for a typical equilibrium deformation predicted by our calculations [see Eq. (28)] and based on the calculations in Ref. [11].

We arbitrarily limit the illustrations to states with $I \leqslant 12$. An unprepared reader might be surprised seeing a perfectly parabolic energy sequence, $E_I \propto I(I+1)$, which, in contrast to similar sequences seen in a huge number of publications, manifests a number of characteristic differences:

(i) The lowest energy perfectly parabolic $E_I \propto I(I+1)$ sequence contains both *even- and odd-spin states*.
(ii) The corresponding sequence referred to as a band contains *states of opposite parities*.
(iii) At certain spins we note the presence of *degenerate energy states*: spin-parity doublets at $I^\pi = 6^\pm, 9^\pm, 10^\pm$ and a degenerate triplet state, composed of a doublet $I^\pi = 12^+$ and a singlet $I^\pi = 12^-$.
(iv) Certain *states are completely missing*: In the present case these are $I^\pi = 1^\pm$, $2^\pm$, and $5^\pm$ states whose energies lie significantly higher and thus do not belong to the illustrated, lowest-energy parabolic sequence.
(v) The calculated spectrum also contains other higher-lying states, which do not join the lowest parabolic sequence and are not discussed here.

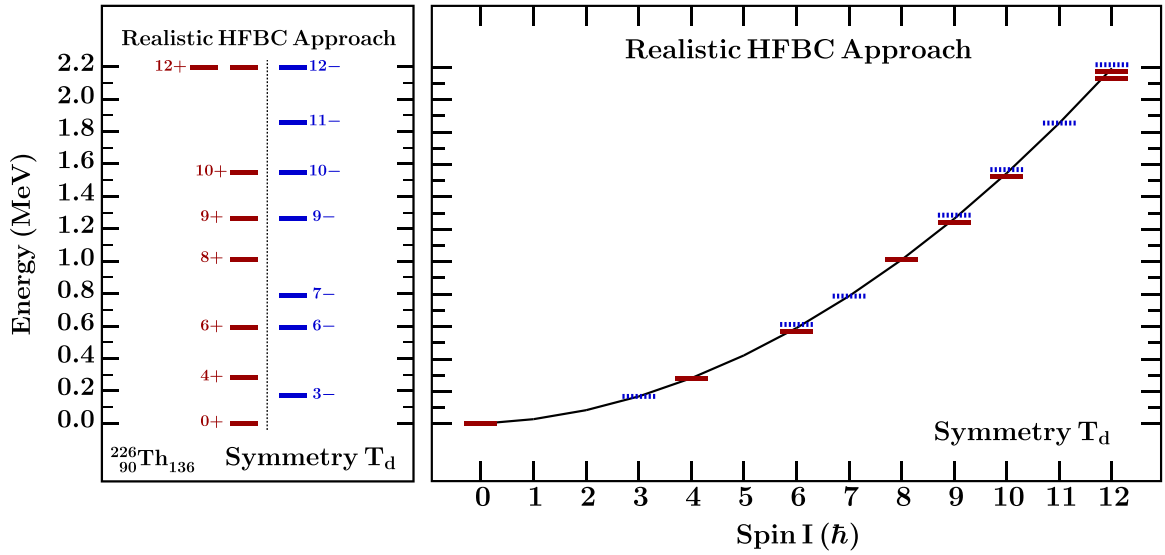

FIG. 17. Results adopted from Ref. [11], showing the structure of the lowest energy E_I vs I sequence obtained within the realistic HFBC formalism, together with spin and parity projection techniques as schematically indicated in Eq. (29) for ^{226}Th. To ensure the link with the T_d symmetry, the HFBC equations were solved under the Q_{32} constraint equivalent to $\alpha_{32} \approx 0.15$; see Eq. (28). For "pedagogical" reasons we use two graphical representations emphasizing, on the left, two structural elements of the problem: the presence of positive and negative parity states in the sequence, and occasional occurrence of degenerate multiplets. On the right, we emphasize the parabolic dependence of energies on spin, $E_I \sim I(I+1)$; the negative parity levels are plotted as dotted lines. Also, the dotted lines should be understood as degenerate with neighboring full lines.

Needless to say, the properties just described are not accidental and take their origin in the structure of one of the irreducible representations of the T_d group as presented next.

3. Irreducible representations of O(3) *and point groups: Band properties of T_d-symmetric nuclei*

The subjects overviewed below have been of interest in molecular physics and chemistry for a long period now, with certain significant publications dating back to the middle of the previous century; see, e.g., Refs. [48–50]. There has been much less interest in the nuclear context. In particular, the nuclear rotation pattern of Fig. 17, was obtained in Ref. [11] using advanced quantum mechanical methods of nuclear physics with neither explicit considerations of symmetries nor group theory. And yet the same pattern can be found in Fig. 138 of Ref. [49] embedded in the discussion of spectra of T_d-symmetric molecules; the monograph in question was published in 1945. We mention in passing that certain nuclear configurations interpreted in terms of α particles can be seen, due to certain geometrical resemblances, as analogous to molecular configurations. This was the case of the 4α cluster T_d configurations of ^{16}O discussed as early as the 1970s and onwards (Refs. [51–54] or more recent ones), and in the cases addressing D_{3h} symmetry in ^{12}C, Ref. [55] and rotation-vibration coupling in ^{16}O, Ref. [56].

To start, let us consider solutions of the rotor problem, Eq. (24). The corresponding wave functions transform as (generally reducible) representations $D^{(I\pi)}$ of the group O(3) in Eq. (26) with definite spin and parity $(I\pi)$. Representations $D^{(I\pi)}$ have the form of $(2I+1)\times(2I+1)$ matrices in the space of rotor wave functions with a given (I^π), whereas construction of irreducible representations involves K mixing with specific combinations of K quantum numbers.

Next, consider a given point group, say G, here in the realization $G = T_d$ as the symmetry of the considered rotor, and let us denote its irreducible representations D_n, for $n = 1, 2, \ldots, \mathcal{N}$. According to standard concepts in group theory (see, e.g., Chapter 3 in Ref. [57]), we can decompose the O(3)-group representations $D^{(I\pi)}$ in terms of the irreducible representations D_n of G, thus providing the link between the rotor states with spin-parity $(I\pi)$ and the point group structures. We demonstrate that

$$D^{(I\pi)} = \sum_{n=1}^{\mathcal{N}} a_n^{(I\pi)} D_n. \tag{30}$$

Alternatively one can write out the "branching rule"

$$D^{(I\pi)} = \bigoplus_{n=1}^{\mathcal{N}} D_n^{\oplus a_n^{(I\pi)}},$$

where $a_n^{(I\pi)}$ are multiplicity factors taking non-negative integer values. Crucially, this is for representations of a given group in terms of representations of a subgroup, in the present case $T_d \subset$ O(3).

Calculating the multiplicity factors needed here is again a standard matter in group theory literature. They are expressed with the help of the characters of irreducible representations

TABLE II. The multiplicity factors $a_n^{(I\pi)}$ belonging to the five irreducible representations of point group T_d for integer spins $I \leqslant 12$ showing separately the results for both parities. The first column lists the irreducible representations. The interested reader may find more details related to point group terminology in the Appendix.

T_d multiplicity factors for $D^{(I\pi=+)}$

I^+	0^+	1^+	2^+	3^+	4^+	5^+	6^+	7^+	8^+	9^+	10^+	11^+	12^+
A_1	1	0	0	0	1	0	1	0	1	1	1	0	2
A_2	0	0	0	1	0	0	1	1	0	1	1	1	1
E	0	0	1	0	1	1	1	1	2	1	2	2	2
F_1	0	1	0	1	1	2	1	2	2	3	2	3	3
F_2	0	0	1	1	1	1	2	2	2	2	3	3	3

T_d multiplicity factors for $D^{(I\pi=-)}$

I^-	0^-	1^-	2^-	3^-	4^-	5^-	6^-	7^-	8^-	9^-	10^-	11^-	12^-
A_1	0	0	0	1	0	0	1	1	0	1	1	1	1
A_2	1	0	0	0	1	0	1	0	1	1	1	0	2
E	0	0	1	0	1	1	1	1	2	1	2	2	2
F_1	0	0	1	1	1	1	2	2	2	2	3	3	3
F_2	0	1	0	1	1	2	1	2	2	3	2	3	3

as follows:

$$a_n^{(I\pi)} = \frac{1}{N_G}\sum_{g\in G}\chi^*_{(I\pi)}(g)\chi_n(g) = \frac{1}{N_G}\sum_{\alpha=1}^{\mathcal{N}} f_\alpha \chi^*_{(I\pi)}(g_\alpha)\chi_n(g_\alpha). \quad (31)$$

According to standard definitions and notation N_G is the order of G, i.e., the number of its elements $g \in G$, and $\chi_{(I\pi)}(g)$ and χ_n are characters of the representations $D^{(I\pi)}$ and D_n, correspondingly. The classes of the point group are enumerated with the index α, the symbol f_α represents the number of elements in each class, and g_α are representative elements for each class. The number of classes equals the number of irreducible representations, $\mathcal{N}$. Using the tables of characters (see, e.g., Refs. [58,59]), one may employ Eq. (31) to obtain the results summarized in Table II.

To proceed towards interpretation of the above information, let us recall that a given matrix of a Hamiltonian invariant under a symmetry group G, e.g., quantum rotor within solutions of given (I^π), can be represented in a block-diagonal form in which blocks correspond to irreducible representations of the group. It follows that there are no off-diagonal matrix elements of the Hamiltonian, which connect states from different representations, expressing the structural fingerprints of the families of states, no matter the values of I, under the condition that they belong to the same irreducible representation. In particular, within each T_d irreducible representation, the lowest-spin state with a specified parity can be treated as the "bandhead" of the sequence of states with increasing spins. Since the structure of the nucleus generating a given rotational band can be seen as predefined by the structure of the ground state, we may interpret the partner states of increasing spins as representing the same intrinsic structure rotating, in classical language, with increasing rotational frequency, and their expected energy vs spin dependence is expected to be quadratic, at least to a leading order.

With the help of the information in Table II we can construct the spin-parity sequences defining the rotational bands built on structurally different ground states corresponding to the T_d irreducible representations listed in the first column of the table. The corresponding solutions are collected in Eqs. (32)–(36):

$$A_1 : I^\pi_{\rm gs} = 0^+,\ 3^-,\ 4^+,\ 6^\pm,\ 7^-,\ 8^+,\ 9^\pm,\ 10^\pm, 11^-,\ 2\times 12^+,\ 12^-,\ldots, \quad (32)$$

$$A_2 : I^\pi_{\rm gs} = 0^-,\ 3^+,\ 4^-,\ 6^\mp,\ 7^+,\ 8^-,\ 9^\mp,\ 10^\mp, 11^+,\ 12^+,\ 2\times 12^-,\ldots, \quad (33)$$

$$E : I^\pi_{\rm gs} = 2^\pm,\ 4^\pm,\ 5^\pm,\ 6^+,\ 7^\pm,\ 2\times 8^\pm,\ 9^\pm, 2\times 10^\pm,\ 2\times 11^\pm,\ 2\times 12^\pm,\ldots, \quad (34)$$

$$T_1 : I^\pi_{\rm gs} = 1^+,\ 2^-,\ 3^\mp,\ 4^\mp,\ 2\times 5^+,\ 5^-,\ 6^+,\ 2\times 6^-, 2\times 7^\mp,\ 2\times 8^\mp,\ 3\times 9^+,\ 2\times 9^-, 2\times 10^+,\ 3\times 10^-, 3\times 11^\mp,\ 3\times 12^\mp,\ldots, \quad (35)$$

$$T_2 : I^\pi_{\rm gs} = 1^-,\ 2^+,\ 3^\pm,\ 4^\pm,\ 5^+,\ 2\times 5^-,\ 2\times 6^+, 6^-,\ 2\times 7^\pm,\ 2\times 8^\pm,\ 2\times 9^+, 3\times 9^-,\ 3\times 10^+,\ 2\times 10^-, 3\times 11^\pm,\ 3\times 12^\pm,\ldots. \quad (36)$$

A few comments linking the above group-theoretic and symmetry-related information and the projected HFBC approach are appropriate at this point. To start, it is expected that the tetrahedral lowest-energy band, referred to as tetrahedral ground-state band, is built on the lowest constrained HFBC $I^\pi = 0^+$ state, called its ground state. Something similar should be said about the T_d-symmetric quantum rotor solutions. The corresponding lowest energy I^π sequence is presented in Eq. (32), giving the symmetry-imposed spin-parity relations in the tetrahedral ground-state band. It turns out that this sequence corresponds exactly to the one obtained earlier, which was based on the projected HFBC formalism and is illustrated in Fig. 17. This simultaneously confirms the intrinsic validity of the formalism and the coherence between the related computer programs and numerical solutions (in full agreement with the group-representation formalism and with the underlying symmetries and their formal description).

It is worth emphasizing at this point that the projected HFBC algorithm and the associated computer program contain no single instructions related to symmetries, symmetry operators, commutation relations, etc. Instead, the only information containing a link with the symmetry environment is implicit, viz., via constraints. Construction of the HFBC solutions satisfying tetrahedral symmetry involves the constraint with the help of the (here tetrahedral) symmetry operator, $\hat{Q}_{32}$. The latter obviously contains no explicit information about spins or parities of the solutions, and yet relations in Eqs. (32)–(36) are produced via projection algorithm. Even if not intuitive, these properties follow the mathematical

background summarized briefly via Eqs. (29)–(31) and exposed in detail in the textbooks of Herzberg, Hamermesh, or Cornwell [49,50,57,59] and also many others, and are well known in molecular physics.

Let us stress that the theorems used here for illustration of the tetrahedral symmetry are formulated using the general language of point groups and therefore not limited to any specific point group. This issue was described in Ref. [11], Fig. 4, illustrating the projected HFBC results for the tetrahedral symmetry case and in Fig. 5 showing the "usual ellipsoidal" symmetry constraint; in the test the tetrahedral constraint was just replaced by the quadrupole one showing a perfect correspondence.

Let us emphasize that the structure represented by Eq. (32) has been confirmed experimentally in Ref. [9]. This, to our knowledge is the first experimental identification of nuclear tetrahedral symmetry concerning a lighter nucleus, ^{152}Sm. The article in question confirms all the essential structural singularities up to spin $I = 10$. This concerns in particular the identification of the parity doublets[1] at $I^{\pi} = 6^{\pm}$, $9^{\pm}$, and $10^{\pm}$ and, what is equally important, the confirmation of the absent states at $I = 1$, 2, and 5 $\hbar$.

Combining the information contained in Eq. (32) with the experimental confirmation in Ref. [9] places the whole sequence of structures predicted in Eqs. (33)–(36) in the category of important experimental challenges. First, the discussed relations represent the full symmetry scheme generated by the T_d group, implying, on the one hand, that identification of any one of them identifies the presence of the discussed symmetry in the corresponding nucleus. On the other hand a confirmation of one of them suggests the presence of any other in the symmetry scheme, whereas certain deviations could indicate the possible symmetry breaking signals, both encouraging, in our opinion, some very interesting and original research possibilities.

On the technical/instrumental level one can imagine at least two complementary strategies. To see their relevance let us recall that at the exact tetrahedral symmetry limit the collective $E2$ and $E1$ type transitions vanish. Consequently the lowest-order collective electric type transitions correspond to a multipolarity $\lambda = 3$: electric octupole transitions. Even though the reduced $B(E3)$ transition probabilities are orders of magnitude weaker than the quadrupole or dipole ones, germanium multidetector systems can be seen as a possible solution, especially since the strict symmetries are seldom realized in nuclei and a partial breaking of those symmetries can produce several interconnecting γ-decay paths including $E1$ and/or $E2$ transitions, which could become detectable.

[1]Strictly speaking, Ref. [9] analyzes a simultaneous presence of tetrahedral *and* octahedral symmetries, the importance of the underlying mechanism being that the tetrahedral group is a sub-group of the octahedral one, O_h. The latter contains inversion, the implication being that the analyzed experimental sequence is in fact composed of two very close-lying parabolas of states with opposite parities, again in perfect agreement with the group-theory affirmations about interrelations between the O_h and T_d groups.

Another instrumentation of choice would be contemporary high resolution mass spectrometry. It is not a paradox that if the electromagnetic signals are weak, the measurement of the masses becomes a natural alternative. In this case the experimental signals would take the form of a series of peaks in counts vs mass (energy) with parabolically increasing distances between the peak positions. Modern instruments, e.g., those at the GSI-Darmstadt, Germany or TITAN, Canada, seem to be the solutions of choice.

Let us complete this part of the discussion with a number of comments which may render links with experimental efforts more efficient. First of all let us notice that we have so far presented the exact T_d-symmetry limit case, which at the same time encourages opening a "new spectroscopy era" by focusing on the bands which are *not* dominated by $E2$ transitions of the $B(E2)$ strengths reaching up to hundred of Weisskopf units. At the same time, we introduced rotational patterns for *all* irreducible representations of the discussed point group. Whereas the first issue can be addressed via efforts employing γ-multidetector systems and high-resolution mass spectrometry, the second one can be hurt by certain traditions in the nuclear structure community, traditions which go back to the middle of the previous century. We refer to the "well-known" (at least in molecular physics) predictions of spectra of the ellipsoidal rotor, which involve as the standard band structure the single $K = 0$ band, accompanied by the doublets of the $K = \pm 1$, $K = \pm 2$, $K = \pm 3$, $K = \pm 4$, ... bands—a sequence which is seldom (if at all) found in the nuclear structure literature. What is usually found instead is evidence limited to the low-K bands, seldom bypassing $K = 3$, the very likely reason being that the corresponding higher-K structures are very difficult to populate. As a not-unlikely consequence it appears that the population difficulty is *de facto* taken for nonexistence.

At this particular point we find a difference compared with molecular physics literature, where the bands with growing K bandheads, combined with the vibration-rotational structures, are numerous and evident. Moreover, rotational bands corresponding to various irreducible representations of molecular point groups, like the ones signaled in Eqs. (33)–(36), are also discussed. At the same time the full rotational structures like the one in Eq. (32) are, to our knowledge, very difficult to evince experimentally in molecular physics for instrumental reasons, and whose discussion certainly bypasses the scope of the present article.

Given all the complications mentioned, combined with the complete absence of evidence in our domain of the discussed structures, we believe that rather than addressing many (or all) of the mathematically identified types of bands it will be of certain advantages to concentrate on the relatively simpler structures like the one of the tetrahedral ground-state band, Fig. 17.

C. Rotation in the presence of C_{2v}, D_{3h}, and D_{2d} octupole symmetries: Band structures deduced with the help of group theory

The extended discussion of the tetrahedral symmetry case in the previous section is supported by the world-first

TABLE III. Similar to Table II but with the multiplicity factors $a_n^{(I\pi)}$ belonging to the four irreducible representations of the point group C_{2v}, for integer spins $I \leqslant 12$ and $\pi = +$. The first column lists irreducible representations of C_{2v}; the interested reader may find details related to the point group terminology in the Appendix.

C_{2v} multiplicity factors for $D^{(I\pi=+)}$

I^+	0^+	1^+	2^+	3^+	4^+	5^+	6^+	7^+	8^+	9^+	10^+	11^+	12^+
A_1	1	0	2	1	3	2	4	3	5	4	6	5	7
A_2	0	1	1	2	2	3	3	4	4	5	5	6	6
B_1	0	1	1	2	2	3	3	4	4	5	5	6	6
B_2	0	1	1	2	2	3	3	4	4	5	5	6	6

experimental evidence in Ref. [9], deduced from experimental data of various authors. It encourages an extension of the analysis of shape-symmetry effects accompanying α_{32} octupole deformation towards α_{31} and α_{33} octupole degrees of freedom which, as presented in the preceding Sections of this article, generate sufficiently well-pronounced potential energy minima, which in many cases may give rise to stable exotic shape configurations.

1. The case of octupole symmetry C_{2v} $\leftrightarrow$ ($\alpha_{31} \neq 0$)

It is sufficient to apply Eqs. (30) and (31) with the characters of the group T_d, replaced by the characters of the group C_{2v} to obtain the results in Tables III and IV. The illustration of the structure of the resulting C_{2v} ground-state band is presented in Fig. 18, analogous to the illustration on the left-hand side of Fig. 17.

2. The case of octupole symmetry D_{3h} $\leftrightarrow$ ($\alpha_{33} \neq 0$)

Analysis of rotational properties of nuclei obeying pure octupole α_{33} geometry and thus containing a threefold symmetry axis as a symmetry element leads to the D_{3h} symmetry. With the help of the group representation theory, we obtain the tables of the multiplicity factors in full analogy to the preceding ones. The corresponding results are collected in Tables V and VI with the slightly modified labeling of the irreducible representations as detailed in the Appendix.

As in the preceding case we will limit ourselves to a short presentation of the ground-state band properties. All the other band structures can be obtained directly, leading to analogs of Eqs. (32)–(36).

TABLE IV. Results similar to the ones in Table III but with multiplicity factors $a_n^{(I\pi)}$ for $\pi = -$.

C_{2v} multiplicity factors for $D^{(I\pi=-)}$

I^-	0^-	1^-	2^-	3^-	4^-	5^-	6^-	7^-	8^-	9^-	10^-	11^-	12^-
A_1	0	1	1	2	2	3	3	4	4	5	5	6	6
A_2	1	0	2	1	3	2	4	3	5	4	6	5	7
B_1	0	1	1	2	2	3	3	4	4	5	5	6	6
B_2	0	1	1	2	2	3	3	4	4	5	5	6	6

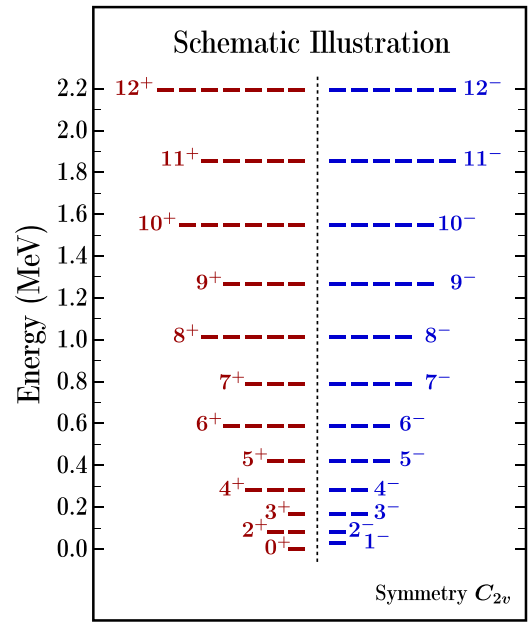

FIG. 18. Graphical representation of the structure of the rotational band built on the $I^\pi = 0^+$ ground state in the case of the symmetry C_{2v}; states $I^\pi = 0^-$ and 1^+ are absent.

The structure of the ground-state band in question is illustrated schematically in Fig. 19, showing the growing degeneracy of multiplets when spin increases. Characteristically, there are no negative parity states allowed in this case for $I \leqslant 2$, and similarly no positive parity states for $I = 3$ and 5. Above $I = 7$ only triplets or higher rank degenerate multiplets are possible. Notice that the predicted structure allows for numerous $E2$ as well as $M1$ transitions, which encourages the use of γ-multidetector systems for a possible identification of such structures in nuclei manifesting the corresponding $\alpha_{33} \neq 0$ potential energy minima.

3. The case of combined $\alpha_{20} \neq 0$ and $\alpha_{32} \neq 0$ shapes: Point group symmetry D_{2d}

Recall that in Sec. III A we introduced the possible breaking of the pure T_d symmetry by competition with the quadrupole α_{20} shape components, leading to yet another symmetry point group, D_{2d}. The resulting multiplicity factors are listed in Tables VII and VIII for positive and negative

TABLE V. Similar to Table III but for the D_{3h} multiplicity factors with $\pi = +$.

D_{3h} multiplicity factors for $D^{(I\pi=+)}$

I^+	0^+	1^+	2^+	3^+	4^+	5^+	6^+	7^+	8^+	9^+	10^+	11^+	12^+
A_1'	1	0	1	0	1	0	2	1	2	1	2	1	3
A_2'	0	1	0	1	0	1	1	2	1	2	1	2	2
E'	0	0	1	1	2	2	2	2	3	3	4	4	4
A_1''	0	0	0	1	1	1	1	1	1	2	2	2	2
A_2''	0	0	0	1	1	1	1	1	1	2	2	2	2
E''	0	1	1	1	1	2	2	3	3	3	3	4	4

TABLE VI. Similar to the preceding table, but for the D_{3h} multiplicity factors with $\pi = -$.

D_{3h} multiplicity factors for $D^{(I\pi=-)}$													
I^-	0^-	1^-	2^-	3^-	4^-	5^-	6^-	7^-	8^-	9^-	10^-	11^-	12^-
A_1'	0	0	0	1	1	1	1	1	1	2	2	2	2
A_2'	0	0	0	1	1	1	1	1	1	2	2	2	2
E'	0	1	1	1	1	2	2	3	3	3	3	4	4
A_1''	1	0	1	0	1	0	2	1	2	1	2	1	3
A_2''	0	1	0	1	0	1	1	2	1	2	1	2	2
E''	0	0	1	1	2	2	2	2	3	3	4	4	4

parities, respectively. Whereas their structures in terms of the irreducible representations are the same as in the T_d case (see the left columns in Tables II and III), the content is totally different, leading to the corresponding $I^\pi = 0^+$ ground-state band illustrated in Fig. 20. Referring to this figure, notice that, characteristically, the $I^\pi = 1^+$ and 3^+ states are totally missing, as are the states $I^\pi = 0^-$ and 1^-. Other than that, the sequence contains an ample selection of both parities and both spin-parity states, which likely lead to the combinations of the $E2$ and $E1$ transitions, whose presence can be seen as a factor encouraging the corresponding experimental identification.

D. Comments about identification of exotic nuclear point group symmetries

Following our mean-field theory potential energy calculations presented in the first part of the article, which manifest strong octupole shell effects, predicted to generate equilibrium deformations with nonvanishing $\alpha_{3\mu}$ components, we

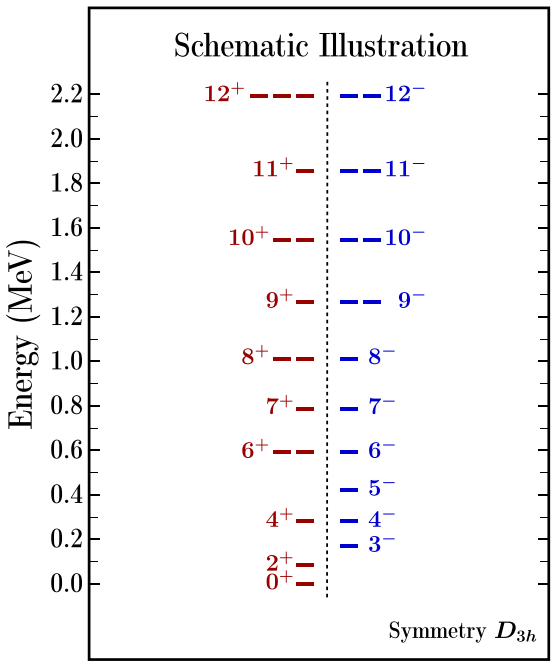

FIG. 19. Illustration similar to that in Fig. 17 but for the structure of the ground-state band in the case of symmetry D_{3h} ($\alpha_{33} \neq 0$).

TABLE VII. The multiplicity factors $a_n^{(I\pi)}$ belonging to the five irreducible representations of the point group D_{2d}, representing the symmetry of nuclear surfaces combining the quadrupole and tetrahedral components α_{20} and α_{32} for integer spins $I \leqslant 12$; here for $\pi = +$.

D_{2d} multiplicity factors for $D^{(I\pi=+)}$													
I^+	0^+	1^+	2^+	3^+	4^+	5^+	6^+	7^+	8^+	9^+	10^+	11^+	12^+
A_1	1	0	1	0	2	1	2	1	3	2	3	2	4
A_2	0	1	0	1	1	2	1	2	2	3	2	3	3
E	0	1	1	2	2	3	3	4	4	5	5	6	6
B_1	0	0	1	1	1	1	2	2	2	2	3	3	3
B_2	0	0	1	1	1	1	2	2	2	2	3	3	3

discussed the physical consequences of such structures implied by the group theory arguments. More precisely, using the applications of point group and group-representation theories very well known from molecular physics literature, we derived the properties of rotational band structures characteristic of each discussed exotic symmetry. Given the fact that tetrahedral symmetry belongs to the most exotic nuclear point group symmetries in the discussed category, and the fact of its experimental identification in the ^{152}Sm nucleus [9], we discussed this particular structure in more detail, but believe that all the predicted structures are worthy of attention and further studies in the future, both from the experimental and theory viewpoints.

Let us emphasize that our focus in this article was on demonstrating the arguments in favor of the presence of the corresponding exotic structures in subatomic physics. This strongly encourages focusing on the exact symmetry limits, in order to define the underlying reference lines in the cleanest, most unperturbed format possible. More advanced analyses are encouraged—taking into account the increasing number of mechanisms such as symmetry breaking and/or coupling with other degrees of freedom, such as collective vibrations—analogous to the molecular structure studies that are numerous in the literature.

Having stressed the strategy of following exact symmetry limits as guidelines, we address possible experiments aiming at the symmetry identification.

1. Experimental focus on collective-level degeneracies

We will first address tests of degeneracies of certain rotational levels as a direct approach to symmetry identification.

TABLE VIII. Similar D_{2d}-symmetry case but for $\pi = -$.

D_{2d} multiplicity factors for $D^{(I\pi=-)}$													
I^-	0^-	1^-	2^-	3^-	4^-	5^-	6^-	7^-	8^-	9^-	10^-	11^-	12^-
A_1	0	0	1	1	1	1	2	2	2	2	3	3	3
A_2	0	0	1	1	1	1	2	2	2	2	3	3	3
E	0	1	1	2	2	3	3	4	4	5	5	6	6
B_1	1	0	1	0	2	1	2	1	3	2	3	2	4
B_2	0	1	0	1	1	2	1	2	2	3	2	3	3

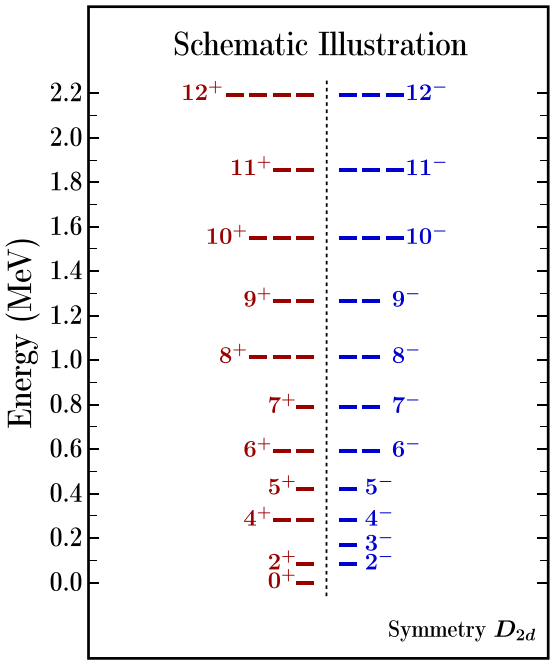

FIG. 20. Schematic illustration of the $I^\pi = 0^+$ ground-state band structure corresponding to the D_{2d} point group symmetry resulting from the combination of the quadrupole α_{20} and octupole α_{32} shape multipolarities. The presented band structure is totally different from the one corresponding to the pure T_d symmetry illustrated in the left-hand side of Fig. 17.

Indeed, in principle, even limiting comparison to the states $I \leqslant 6$ in Figs. 17–20 allows us to distinguish between patterns illustrated in a unique manner. Yet, such a strategy will be subject to a number of limitations, which influence the final choices:

(i) To begin with, nuclei selected as experiment candidates should correspond to a compromise between theory criteria of the strongest manifestations of symmetry, such as the Z vs N combination with the most pronounced local potential energy minima, and the experimental criteria guided by the optimal beam/target combinations and instrumental detection efficiency. It follows that the discussed compromises will very likely guide the final choice, deviating from the strongest symmetry manifestation cases with the result that ideal, exact degeneracies will be to an extent perturbed.

(ii) Consider a given d-fold degenerate multiplet at a given spin-parity condition, I^π. The related wave functions, $\Psi^{I\pi}_{M,\rho}$ for $\rho = 1, 2, \ldots, d$ are mutually orthogonal, representing independent substructures. Consequently, the feeding conditions of each of the multiplet members should be expected to differ, perhaps strongly from one multiplet member to another, with the result that identification of some of them could become difficult and some multiplet members could be missing in single-experiment data.

After enumerating certain difficulties which can be expected, let us also recall a strongly helping factor: All band members discussed here form parabolic E_I-vs-I dependence; see Fig. 5 in Ref. [9] for illustration. This quadratic dependence is likely to play a very helpful role in eliminating or accepting certain experimental levels as band/multiplet members, especially when feeding transitions are weak and spin-parity identifications of levels are uncertain.

2. Experimental focus on single-particle fourfold level degeneracies: Tetrahedral symmetry case

After a brief discussion of perspectives of identification of nuclear symmetries via collective rotational I^π level degeneracies, let us turn to yet another very attractive and exotic quantum mechanism, which to our knowledge has so far never been addressed experimentally. This is the predicted existence of fourfold nucleonic level degeneracies.

So far, we have discussed the properties of even-even nuclei, therefore deduced from the properties of the groups T_d, C_{2v}, D_{3h}, and D_{2d}, rather than their double-group partners. In the case of mean-field solutions where the direct objects of interest are fermions and the related single-nucleon excitation energies, the symmetry properties are described in terms of the double point groups T_d^D, C_{2v}^D, D_{3h}^D, and D_{2d}^D. All the irreducible representations of the latter are two dimensional, implying a Kramers time-reversal double degeneracy, with the exception of the T_d^D group having two two-dimensional and one four-dimensional irreducible representations. It then follows that among the single-particle levels of the corresponding nuclei some are fourfold degenerate.

In the case of a static (no rotation) mean-field theory each single-particle eigenvalue, e_ν, is common to both ψ_ν and its time-reversed image $\psi_{\bar\nu} \equiv \hat T \psi_\nu$, where $\hat T$ denotes the time-reversal operator, and we have

$$\hat H \psi_\nu = e_\nu \psi_\nu \quad \text{and} \quad \hat H \psi_{\bar\nu} = e_{\bar\nu} \psi_{\bar\nu} \quad \text{with } e_\nu = e_{\bar\nu}. \tag{37}$$

Since solutions ψ_ν and $\psi_{\bar\nu}$ are linearly independent, to each particle-hole excitation of an even-even nucleus,

$$\delta e^*_{\text{1p-1h}} \leftrightarrow e_\mu - e_\nu = e_\mu - e_{\bar\nu} = e_{\bar\mu} - e_\nu = e_{\bar\mu} - e_{\bar\nu}, \tag{38}$$

with ψ_ν and $\psi_{\bar\nu}$ originally occupied and ψ_μ and $\psi_{\bar\mu}$ unoccupied, there correspond four linearly independent particle-hole configuration wave functions constructed out of the appropriate combinations between the pairs: $\{\psi_\nu \text{ or } \psi_{\bar\nu}\}$ and $\{\psi_\mu \text{ or } \psi_{\bar\mu}\}$. It follows that, in the nonspherical even-even nuclei whose symmetry point group is *neither* T_d^D *nor* O_h^D, to each particle-hole excitation energy there corresponds a fourfold degeneracy caused by the presence of four linearly independent 1p-1h wave functions, but manifested by a *single* excitation energy, $\delta e^*_{\text{1p-1h}}$; see Eq. (38).

In the presence of fourfold single-nucleon degeneracies we should think of totally new spectroscopic challenges. Indeed, in this case, we have to consider the wave functions, say, ψ_{ν_1}, $\psi_{\bar\nu_1}$, ψ_{ν_2}, and $\psi_{\bar\nu_2}$ (in place of ψ_ν and $\psi_{\bar\nu}$ introduced previously) accompanied by ψ_{μ_1}, $\psi_{\bar\mu_1}$, ψ_{μ_2}, and $\psi_{\bar\mu_2}$ (in place of ψ_μ and $\psi_{\bar\mu}$). Assuming that the associated ν-type fourfold degenerate energy level is occupied and the μ-type remains unoccupied, we can construct

(i) one-particle one-hole excitations leading to 16 linearly independent, mutually orthogonal wave functions, or
(ii) two-particle two-hole excitations leading to 32 linearly independent, orthogonal wave functions.

Yet, in the exact symmetry limit all these combinations correspond either to the *single* excitation energy equal to $\delta e^*_{\text{1p-1h}}$ of Eq. (38) in the case of one-particle one-hole excitations or to a *single* excitation energy $\delta e^*_{\text{2p-2h}}$ in the case of two-particle two-hole excitations and equal to twice the single-particle energy difference, i.e., $2 \times (e_{\mu_1,\mu_2} - e_{\nu_1,\nu_2})$.

However, in contrast to the strict mathematical results, it is very unlikely that in the realistic physics cases, even for the very well pronounced potential energy minima, the discussed T_d^D symmetry will be exact. Consequently each of the fourfold degenerate levels, above referred to as e_{ν_1,ν_2} and e_{μ_1,μ_2} within the exact symmetry, in a slightly broken symmetry case is expected to undergo a splitting into two close-lying single-particle levels,

$$\text{Exact } T_d^D: \ \{e_{\nu_1,\nu_2}; e_{\mu_1,\mu_2}\} \ \rightarrow \ \{e_{\nu_1}, e_{\nu_2}; e_{\mu_1}, e_{\mu_2}\}, \quad (39)$$

leading to four slightly different $\delta e^*_{\text{1p-1h}}$-type excitation energies and eight slightly different $e^*_{\text{2p-2h}}$-type energies. Experimentally we arrive at challenges of identifying either 16-plets of 1p-1h excited states or 32-plets of 2p-2h excited states with close-lying energies, but with generally different spins.[2] One should expect numerous weak (single-particle strength) electromagnetic transitions feeding or depopulating those numerous states, certain among them forbidden by the usual electromagnetic selection rules.

To summarize,

> *It is worth emphasizing that the priority in the discussed problem is to obtain evidence for the relatively large number of close-lying exited states rather than focusing on the complete determination of the full quadruplets or octuplets of nearly degenerate particle-hole excited states. An evidence of a few such excitations will provide encouraging evidence of the fourfold T_d^D degeneracies and a good starting point for more advanced theory studies.*

When planning experimental identification of the discussed particle-hole excitation high-level degeneracies we have an extra obstacle to take care of: distinguishing between the sought signals (coming from the particle-hole excitations generated by the tetrahedral symmetry configuration) and the fake signals (possibly coming from particle-hole excitations of the competing, e.g., superdeformed minima), predicted to be close in energy. We will have a closer look at this aspect next.

Indeed, in nuclei with all neutron levels below the large $N = 136$ tetrahedral gap occupied, the $I^\pi = 0^+$ tetrahedral ground states are expected to generate relatively *high-lying* one-particle one-hole or two-particle two-hole excitations with nearly degenerate excitation energies. Such excitations will be energetically separated from the particle-hole excitations originating from the competing axial-symmetry quadrupole minima. As it turns out, the superdeformed minima are predicted to be very close in the energy scale to the tetrahedral ground states studied in this article; they are expected to be populated with comparable probabilities. Because of this systematic energy difference one may hope to avoid overlapping between the T_d^D highly degenerate spectra of close-lying particle-hole excitations and the other ones, originating incidentally from totally different, quadrupole-deformed shape configurations.

3. Missing states as symmetry identifiers

Experimental verification of nonexistence of certain physical facts is a very difficult issue and in many situations next to impossible, being directly related to the sensitivity of the instrumentation used. In fact this problem can generally be discussed in relative terms only. From reading Figs. 17–20 we predict an absence of certain (usually low-spin) states, which should be missing in the illustrated parabolic sequences associated with the selected irreducible representations. However, we might expect the presence of contaminating signals originating from levels with the right spin-parity combinations, but whose energies incidentally lie in the studied excitation zones of interest. The question arises, which extra arguments and criteria can possibly be applied in order to diminish the probability of contaminating the true results? Some ideas will be discussed next.

In the present context we can expect a few sources of structural contamination belonging to two classes: collective and noncollective excitations. Collective rotation signals may originate either from exotic symmetry minima or from the competing prolate-oblate quadrupole symmetry states, possibly superdeformed. Since the latter ones should be characterized by large moments of inertia and reduced transition probabilities of the order of dozens to hundreds of Weisskopf units, the signals of this type should become easily eliminated. The collective rotation signals coming from the exotic symmetry minima could in principle be also recognized because the predicted parabolic energy vs spin sequences originating from various irreducible representations are characterized both by different energy bandheads and by different effective moments of inertia.

As far as a possible competition from the collective vibrational states is concerned, the latter are expected in the 1 MeV energy range and therefore should not interfere with the low-spin rotational transitions in most of the cases of interest.

Let us consider two other sources of possible contamination, originating from noncollective (particle-hole) excitations, either from competing prolate-oblate deformed axial-symmetry minima or from the exotic symmetry minima in question. In the case of the former, we will encounter relatively well-known mechanisms of irregular energy vs spin excitation patterns, which due to the axial symmetry and the implied K quantum number conservation lead to the presence of the so-called K isomers and yrast-trap energy pockets. An

[2]More precise theory information about spins and parities of such states may be provided within mean-field theory after employing the angular momentum and parity projections techniques which are considered standard today. Yet, the presence of numerous configurations to take into account enforces this type of study to follow the "case by case" strategy rather than massive calculations.

encouraging element of the discussion at this point is provided by the fact that such structures can be very well treated on theory grounds either within the realistic mean-field approach employing the so-called tilted Fermi surface method (see, e.g., Ref. [1]) or with the spherical shell-model approach. Even though the proposed elimination procedure is to an extent a model-dependent one, if the suspected contaminant states can be shown to belong to a decay scheme containing K isomers, their interpretation as axially symmetric structures will remain very likely.

The remaining, third source of difficulty is excluding a possible misinterpretation due to an incidental presence of a state with a predefined spin-parity combination arriving at the parabolic energy zone while being, in fact, a particle-hole excited state of, e.g., the $I^\pi = 0^+$ exotic symmetry ground state. We believe that in this context coincidentally positive signals are very unlikely. First, it is wellknown that the particle-hole excitation energies are very irregular and it is very unlikely that the corresponding energy fits the energy position at the parabola within a few keV interval. Second, the corresponding total nuclear spins and parities result from combinations of nucleonic spins and parities of levels existing in the vicinity of the Fermi level, and again we find it very unlikely that the strict energy and spin conditions would fit coincidentally.

4. Electromagnetic transitions to trace symmetries: General remarks

Analysis of the electromagnetic transition properties belongs to the most powerful nuclear structure tools, yet its complexity in the present context bypasses the complexity of the spectral problems discussed in this article. This is because when analyzing the transitions we will be confronted with a number of extra quantum mechanisms which are less important or nonexisting in the case of examining the spectral properties.

The first element of the discussion can be formulated as follows. There exists an important difference between the arguments of symmetry from the viewpoint of mathematics vs the same issue seen through the perspective of physics. Indeed, the symmetry conditions at the constraint of $\langle Q_{32}\rangle = q_{32}$ and $\langle Q_{32}\rangle = q'_{32}$ are strictly the same, that is to say, spatial density distributions are invariant under the same symmetry elements in both cases. The same is not at all true in case of the physics solutions, as discussed in detail in Ref. [11] [the interested reader may compare Figs. 4(a)– 4(f) for the tetrahedral symmetry case and Figs. 5(a)– 5(f) for the quadrupole-axial symmetry case]. An increase in the constraint values impacts markedly the energies of the states, what alerts us about the modifications in the structures of the wave functions, solutions of the related Schrödinger equation. It follows that the matrix elements of, in particular, electromagnetic transition operators will vary with increasing strengths of the constraints at symmetry fixed, and some extra control mechanisms need to be introduced to quantify those effects.

The second degree of freedom in the discussed context is the dynamical symmetry breaking via collective zero-point motion in the deformations competing with the symmetry driving ones, e.g., α_{20} and α_{22} competing with $\alpha_{3\mu}$. For instance, in the exact tetrahedral symmetry limit, the reduced transition probabilities of the collective $E2$ as well as $E1$ transitions vanish and consequently none of those should be expected among the levels in Fig. 17. If, however, large amplitude quadrupole oscillations would be allowed around $\alpha_{20} = 0$ and $\alpha_{22} = 0$ equilibrium points, the dynamical (most probable) quadrupole deformations and related $B(E2)$ values will be altered (thus nonvanishing) and the electromagnetic decays connecting levels of the spectrum in Fig. 17 will be altered accordingly. One can control this type of problem by solving realistically the problem of collective nuclear motion. Encouraging steps in this directions via expanding the microscopic reformulation of the problem of adiabaticity and of the Bohr model have been published recently [40] and the corresponding analysis is in progress.

As we can see, electromagnetic transition analysis is an important but complex problem in research of exotic-symmetries; fortunately it can be treated at an independent, advanced step, provided that some signals of symmetries have been found from the energy-spectrum tests.

V. SUMMARY AND CONCLUSIONS

Nuclear deformations and the implied geometrical symmetries are very often addressed in the literature. These concepts owe their existence to the short range of the strong interactions which, combined with the compactness of the nuclear density spatial distribution allow for introducing the notion of a nuclear surface and the associated geometry. It turns out that the shapes of nuclear surfaces can be described as deviations from a spherical one, and therefore conveniently represented with the help of multipole expansions of multipolarities $\lambda = 2$ (quadrupole), $\lambda = 3$ (octupole), $\lambda = 4$ (hexadecapole), etc., with the spherical harmonics $\{Y_{\lambda\mu}\}$ serving as an expansion basis. Whilst quadrupole deformations $\{\alpha_{20}, \alpha_{22}\}$ are in the majority of studied cases of leading importance, interestingly enough this rule is broken by the next order multipoles, $\{\alpha_{30}, \alpha_{31}, \alpha_{32}, \alpha_{33}\}$ in heavy lead isotopes and neighboring nuclei placed "northeast" from ^{208}Pb in the nuclear mass chart.

In the present article we have addressed the consequences of the fact that, in the heavy nuclei mentioned, these are octupole deformations which are the first nonvanishing ones to describe deviations from sphericity with increasing neutron and proton numbers, generating well pronounced minima on the potential energy surfaces. The underlying shell effects to the leading order are caused by the strong repulsion between neutron $2g_{9/2}$ and $1j_{15/2}$ orbitals, whose orbital angular momentum quantum numbers ℓ satisfy $\Delta\ell = 3$ and produce strong matrix elements in terms of $\hat{Q}_{\lambda=3} \cdot \hat{Q}_{\lambda=3}$ (octupole-octupole) residual interactions, or, alternatively, repulsion caused by octupole deformations in the mean-field Hamiltonian.

The neutron $2g_{9/2}$ and $1j_{15/2}$ orbital repulsion leads to very strong shell effects, generating what we call the $N = 136$ "universal octupole magic number," or, alternatively, the "fourfold octupole magic number" emphasizing in this way the presence of strong neutron gaps at all four nonzero octupole deformations, with the sizes nearing $\Delta e \approx 3$ MeV in the strongest α_{32} deformation case. Whereas the

axial-symmetry pear-shape generating α_{30} deformation produces very well-known effects of, among others, octupole parity-doublet bands, which have been studied over the years, the effects of the other octupole degrees of freedom can be considered *de facto* unknown. Interestingly, the shapes generated either by a pure α_{31} deformation or its combination with the axial quadrupole, $\{\alpha_{20}, \alpha_{31}\}$, lead to a C_{2v} point group symmetry of the nuclear surface, whilst α_{33} alone, or in the combination $\{\alpha_{20}, \alpha_{33}\}$, leads to D_{3h} symmetry. In contrast, α_{32} alone produces shapes with tetrahedral symmetry T_d while its combination with the quadrupole-axial deformations leads to the D_{2d} point group symmetry.

This article focuses on nuclear structure implications of the predicted nuclear point group symmetries C_{2v}, D_{3h}, T_d, and D_{2d}. They are referred to as *exotic* given the fact that to our knowledge they were either not addressed in the nuclear structure literature, or their experimental evidence is as scarce as in the case of T_d symmetry.

To obtain information about shape competition and coexistence we employed a phenomenological, realistic mean-field approach together with the macroscopic-microscopic method. We used the Hamiltonian with the deformed "universal" [26,27] Woods-Saxon potential together with the newly determined potential parameters from Ref. [25]. Parameter adjustment was based on the recent experimental data, the inverse problem theory of applied mathematics, and Monte Carlo simulations. This approach allowed us to eliminate parametric correlations and to increase in this way the stability of predictions outside of the fitting zones, i.e., in particular when addressing the new zones of interest.

Our mean-field calculations were performed in the space of deformation parameters including α_{20} and α_{22} in the quadrupole sector, $\alpha_{3\mu=0,1,2,3}$ in the octupole sector, and α_{40} (occasionally α_{42} and α_{43}) in the hexadecapole one. They were performed within 3D and 4D deformation meshes, a typical subspace involving between 5×10^6 and 5×10^7 deformation points per mesh. Within each 4D mesh several bidimensional $(\alpha_{\lambda\mu}, \alpha_{\lambda'\mu'})$ combinations were constructed to produce graphical representations of the results in the form of contour plots. For instance, in the case of the 4D mesh $(\alpha_{20}, \alpha_{22}, \alpha_{40}, \alpha_{42})$ we found particularly instructive projections $(\alpha_{20}, \alpha_{22})_{\text{min: }\alpha_{40},\alpha_{42}}$, $(\alpha_{20}, \alpha_{40})_{\text{min: }\alpha_{22},\alpha_{42}}$, $(\alpha_{22}, \alpha_{40})_{\text{min: }\alpha_{20},\alpha_{42}}$, and $(\alpha_{40}, \alpha_{42})_{\text{min: }\alpha_{20},\alpha_{22}}$. Results from various 4D subspaces of the eight-dimensional deformation space allowed for constructing a database composed of over 10^4 various 2D projections, constituting a powerful source of information which allows for overlooking the evolution of various shape properties. In particular, in the (Z, N) zone of interest in this article we only found weak effects of the quadrupole triaxiality (α_{22}), facilitating the analysis of the direct competition between the quadrupole and octupole degrees of freedom.

In the next step we analyzed total energy projections involving competition between quadrupole and octupole deformations, $(\alpha_{20}, \alpha_{3\mu})$, minimized over α_{40}, the latter option as a step towards more realistic predictions. Calculations predict the strongest exotic symmetry effects for T_d symmetry, $(\alpha_{20} = 0, \alpha_{32})$, especially in ^{220}Po and ^{222}Rn, and slightly weaker ones in ^{224}Ra and ^{226}Th, all isotones of the universal octupole magic number $N = 136$. Similar can be said about the D_{3h} symmetry in the above $N = 136$ isotones, even though the potential barriers surrounding the minima in question are systematically slightly lower. In all these nuclei, the minima become less pronounced with N departing from the magic $N = 136$ configuration.

The C_{2v} symmetry is predicted to appear in three forms: the one in lighter nuclei, Pb and Po, with configurations similar to those just mentioned, i.e., of double minima of the $(\alpha_{20} = 0, \alpha_{31})$ type; in heavier nuclei in the form of double minima superposed with quadrupole oblate shapes, $(\alpha_{20} < 0, \alpha_{31})$; or alternatively in the form of long valleys, $(\alpha_{20} > 0, \alpha_{31})$, parallel to the α_{31} axis. Those latter configurations are expected to generate collective vibrations and lead to dynamical C_{2v} equilibrium.

To address the issue of experimental identification of the theoretically predicted exotic symmetries, following earlier experience obtained by combining the spin-parity projected Hartree-Fock-Bogolyubov mean-field theory, with the symmetry and group theory considerations from Ref. [11], we have analyzed the rotational band properties expected from nuclei with the corresponding symmetries. The mathematical techniques used by us follow the ones very well known from molecular physics, but are seldom used in the microscopic, e.g., mean-field calculations, Refs. [11] and [9] being exceptions. The main results, presented in a compact way in Figs. 17–20 were limited to the structures of bands built on the $I^\pi = 0^+$ bandheads, but the information provided allows one to reconstruct the full information; the interested reader can simply follow the pattern detailed for the T_d case, Eqs. (32)–(36).

The most important predictions applicable in symmetry identification analyses can be summarized as follows:

(i) Each of the discussed exotic symmetries generates distinct structures in terms of the energy vs spin-parity sequences, $\{E_{I^\pi}\}$, which differ significantly from the well-known properties of ellipsoidal rotors.
(ii) At certain spins we predict degeneracies: sometimes at positive parities, sometimes at negative parities, and sometimes with both parities ("degenerate rotational multiplets").
(iii) At some spin-parity combinations, depending on the symmetry point group, no states are allowed.

These characteristic features are distinct from one point group to another (see Figs. 17–20), therefore if confirmed experimentally, they would identify the sought quantum symmetries.

Since the strict applications of the formal criteria just recalled may lead to severe experimental difficulties (for instance, identifying fivefold degeneracy at $I^\pi = 5^\pm$ in the C_{2v}-symmetry case, Fig. 18) we developed some more detailed arguments showing how to identify the sought symmetry *without identification of all the items* in the criterion list.

Theory predictions excluding the presence of certain I^π states in an examined rotational band can be seen as precious and powerful criteria helping identification of the symmetry,

but the experimental confirmation of the absence usually depends on the actual instrumental sensitivity and may change with improvement of the instrumentation. Since this particular problem does not have a solution (in any branch of physics), we included a discussion of mechanisms which can help the identification at a given instrumental sensitivity level.

ACKNOWLEDGMENTS

J.D., H.L.W., and J.Y. would like to acknowledge partial support by the Polish National Science Centre under Contract No. 2016/21/B/ST2/01227. H.L.W. acknowledges partial support via the National Natural Science Foundation of China (Grant No. 11975209) and the Physics Research and Development Program of Zhengzhou University (Grant No. 32410017). Partial support from French-Polish collaboration COPIN, No. 04-113 and No. 05-119 and COPIGAL, is acknowledged.

APPENDIX: VOCABULARY OF POINT GROUP NOTATION USED IN THIS ARTICLE

Below we recall selected definitions and notation to facilitate reading certain fragments of this article for persons using neither group nor point group techniques on an everyday basis.

1. Notation related to point groups

We begin by recalling that all point groups, G, are composed of elements $g_1, g_2, \ldots, g_{\mathcal{N}_G} \in G$, defined as symmetry operations acting on finite-size objects in 3D space, like molecules or nuclei. By definition, they all leave at least one point of the considered object invariant. It follows that all corresponding symmetry elements can be composed of rotations $\hat{C}_n$ through angles $\alpha_n = 2\pi/n$ about a common axis and mirror reflections in planes $\hat{\sigma}$. In particular, space inversion $\hat{I}$ and rotary-reflection axis operations $\hat{S}_n \equiv \hat{C}_n \circ \hat{\sigma}$ can be expressed as combinations of the above elements.

Traditionally, the largest-n symmetry axis is called "vertical," e.g., a threefold one, $\hat{C}_{3v}$, the reflections in a plane perpendicular to $\hat{C}_{nv}$ are called "horizontal," $\hat{\sigma}_h$, and those in a plane passing through the axis are called "vertical," $\hat{\sigma}_v$. We mention a special case used in the text, $\hat{\sigma}_d$, a reflection in a plane containing the principal axis of symmetry and bisecting the angle between two twofold rotation axes perpendicular to the principal axis, required for the D_{2d} group.

2. Notation related to irreducible representations

There exist a number of typographical conventions related to the way of writing the symbols associated with certain irreducible representations. The one-dimensional even and odd representations referring to the $\hat{C}_2$-symmetry element are usually denoted with letters A and B, respectively. Various representations of the same symmetry are distinguished with the index, e.g., three one-dimensional even representations will be denoted A_1, A_2, and A_3, respectively. The two-dimensional representations are traditionally denoted E and the three-dimensional ones F. A similar convention of indexing applies if there are more than one of each appearing in the discussion, e.g., E_1 and E_2 and/or F_1 and F_2 etc.

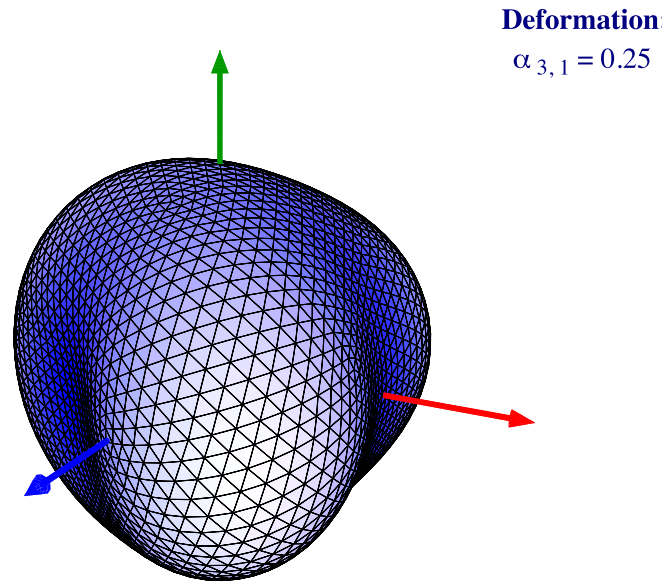

FIG. 21. Illustration of the surface symmetry at deformation $\alpha_{31} = 0.25$ representing an example of the C_{2v} group. The axis pointing to the right is the $\mathcal{O}_x$ axis, the twofold symmetry axis in the present case.

In particular, when the symmetry element list contains inversion $\hat{\mathcal{I}}$, an index g (from German "gerade," even) or u (from German "ungerade," odd) can be added to the representation symbols, e.g., A_g, A_u, and B_u means, erspectively, the irreducible representations even with respect to the $\hat{C}_2$ rotation and even with respect to inversion, even with respect to rotation and odd with respect to inversion, and finally odd with respect to rotation and odd with respect to inversion.

When the operation in question is $\hat{\sigma}_h$, the even and odd representations are sometimes distinguished by prime and double-prime symbols, respectively. For instance, A' and B'' signify the representations even with respect to $\hat{C}_2$ and $\hat{\sigma}_h$ and odd with respect to both of these elements.

We will briefly recall the definitions of the C_{2v}, D_{2d}, and D_{3h} point groups discussed in this article; presentation of the T_d group would require certain extra notational complications and is omitted here, especially since this particular group is among the most often addressed and illustrated in the literature, in particular in the context of symmetries of molecules.

3. Point group C_{2v}

This is a particular case of the C_{nv} group which contains a rotation axis of order n, $\hat{C}_n$, and a "vertical" symmetry plane, $\hat{\sigma}_v$, which passes through this axis. It follows that there are n symmetry planes and $2n$ elements in total. For $n = 2$ we find the four-element group

$$C_{2v} = \left\{\mathbb{1}, \hat{C}_2, \hat{\sigma}_v^{(1)}, \hat{\sigma}_v^{(2)}\right\}, \tag{A1}$$

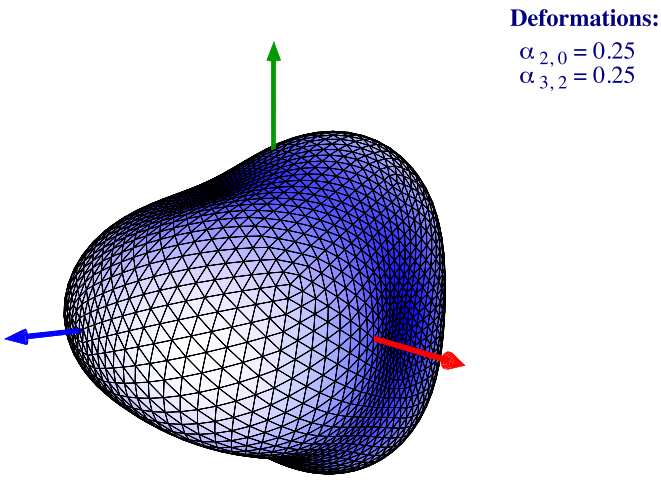

FIG. 22. Illustration of a surface with an arbitrary choice of the combination $\alpha_{20} = 0.25$ and $\alpha_{32} = 0.25$ representing an example of the D_{2d} group.

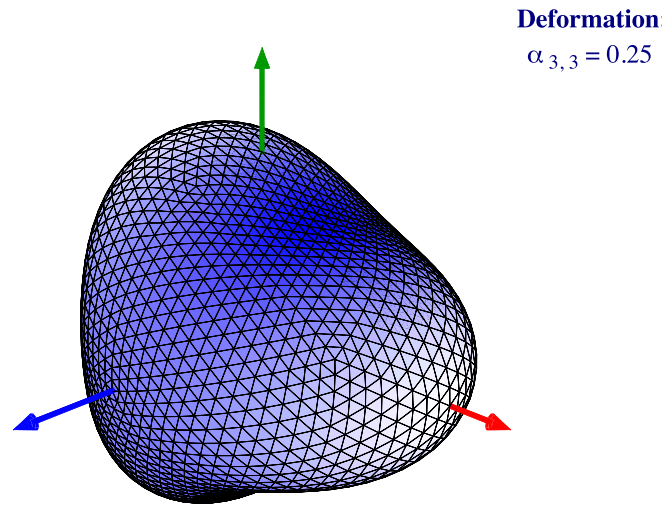

FIG. 23. Illustration of the nuclear surface at $\alpha_{33} = 0.25$ representing an example of the D_{3h} symmetry. The axis pointing to the left is the $\mathcal{O}_z$ axis, marking the threefold rotation symmetry in this case.

where $\mathbb{1}$ is the neutral element. Note that the second reflection element is generated by a consecutive reflection and rotation, $\hat{\sigma}_v^{(2)} = \hat{C}_2 \circ \hat{\sigma}_v^{(1)}$. An example of a C_{2v} symmetric surface is shown in Fig. 21.

4. Point group D_{2d}

The group D_{2d} is a particular case of D_{nd} which contains one n-fold axis, C_n, and one horizontal twofold axis, U_2, where $(n-1)$ images of the U_2 axis are also generated, giving n U_2-type axes altogether.

By definition we add a vertical symmetry plane, $\hat{\sigma}_d$, passing midway between the two neighboring U_2-type axes, thus obtaining n of those symmetry planes in total (the symbol d stands for "diagonal"). Finally, the combinations $\hat{C} \circ \hat{\sigma}_d$ generate n rotary reflections $\hat{S}$. Group D_{nd} contains $4n$ operations in total. For the particular case $n = 2$ we find

$$D_{2d} = \{\mathbb{1}, \hat{C}_2, \hat{U}_2^{(1)}, \hat{U}_2^{(2)}, \hat{\sigma}_d^{(1)}, \hat{\sigma}_d^{(2)}, \hat{S}_4, \hat{S}_4^3\}. \tag{A2}$$

An illustration of a D_{2d} symmetric surface is shown in Fig. 22.

5. Point group D_{3h}

This group is a particular case of the D_{nh} group containing a rotation axis of order n, $\hat{C}_n$, and a second-order axis perpendicular to the former, $\hat{U}_2$. Consequently there are n such axes of the second order, $\{\hat{U}_2^{(1)}, \hat{U}_2^{(2)}, \ldots, \hat{U}_2^{(n)}\}$. Moreover, it contains a vertical symmetry plane, $\hat{\sigma}_v$, and thus n corresponding images, $\{\hat{\sigma}_v^{(1)}, \hat{\sigma}_v^{(2)}, \ldots, \hat{\sigma}_v^{(n)}\}$. The group also contains a horizontal symmetry plane, $\hat{\sigma}_h$, which combined with C_n leads to the sequence $\hat{C}_n \circ \hat{\sigma}_h$, $\hat{C}_n^2 \circ \hat{\sigma}_h$, $\ldots$, $\hat{C}_n^n \circ \hat{\sigma}_h$. This group contains $\mathcal{N}_G = 4n$ group elements in total.

By setting $n = 3$ we arrive at the D_{3h} group containing $4n = 12$ elements,

$$D_{3h} = \{\mathbb{1}, \hat{C}_3, \hat{C}_3^2, \hat{U}_2^{(1)}, \hat{U}_2^{(2)}, \hat{U}_2^{(3)}, \hat{\sigma}_h, \hat{\sigma}_v^{(1)}, \hat{\sigma}_v^{(2)}, \hat{\sigma}_v^{(3)}, \hat{C}_3 \circ \hat{\sigma}_h, \hat{C}_3^2 \circ \hat{\sigma}_h\}. \tag{A3}$$

An illustration of a D_{3h} symmetric surface can be found in Fig. 23.

[1] M. J. A. de Voigt, J. Dudek, and Z. Szymański, Rev. Mod. Phys. **55**, 949 (1983).
[2] K. Heyde and J. L. Wood, Rev. Mod. Phys. **83**, 1467 (2011).
[3] J. L. Wood, K. Heyde, W. Nazarewicz, M. Huyse, and P. V. Duppen, Phys. Rep. **215**, 101 (1992).
[4] K. Heyde, P. V. Isacker, M. Waroquier, J. L. Wood, and R. A. Meyer, Phys. Rep. **102**, 291 (1983).
[5] W. Nazarewicz, P. Olanders, I. Ragnarsson, J. Dudek, G. A. Leander, P. Möller, and E. Ruchowska, Nucl. Phys. A **429**, 269 (1984).
[6] W. Nazarewicz, G. A. Leander, and J. Dudek, Nucl. Phys. A **467**, 437 (1987).
[7] I. Ahmad and P. A. Butler, Annu. Rev. Nucl. Part. Sci. **43**, 71 (1993).
[8] P. A. Butler and W. Nazarewicz, Rev. Mod. Phys. **68**, 349 (1996).
[9] J. Dudek, D. Curien, I. Dedes, K. Mazurek, S. Tagami, Y. R. Shimizu, and T. Bhattacharjee, Phys. Rev. C **97**, 021302(R) (2018).
[10] J. Dudek, J. Dobaczewski, N. Dubray, A. Góźdź, V. Pangon, and N. Schunck, Int. J. Mod. Phys. E **16**, 516 (2007).
[11] S. Tagami, Y. R. Shimizu, and J. Dudek, Phys. Rev. C **87**, 054306 (2013).
[12] L. M. Robledo and P. A. Butler, Phys. Rev. C **88**, 051302(R) (2013).
[13] K. Nomura, D. Vretenar, T. Niksic and B.-N. Lu, Phys. Rev. C **89**, 024312 (2014).

[14] K. Nomura, R. Rodríguez-Guzmán, Y. M. Humadi, L. M. Robledo, and J. E. García-Ramos, Phys. Rev. C **102**, 064326 (2020).

[15] K. Nomura, L. Lotina, T. Niksic, and D. Vretenar, Phys. Rev. C **103**, 054301 (2021).

[16] K. Nomura, R. Rodríguez-Guzmán, L. M. Robledo, and J. E. García-Ramos, Phys. Rev. C **103**, 044311 (2021).

[17] A. V. Afanasjev, H. Abusara, and S. E. Agbemava, Phys. Scr. **93**, 034002 (2018).

[18] P. Jachimowicz, M. Kowal, and J. Skalski, Phys. Rev. C **95**, 034329 (2017).

[19] J. Dudek, T. R. Werner, and Z. Szymański, Phys. Lett. B **248**, 235 (1990).

[20] X. Li, J. Dudek, and P. Romain, Phys. Lett. B **271**, 281 (1991).

[21] W. Nazarewicz, P. Olanders, I. Ragnarsson, J. Dudek, and G. A. Leander, Phys. Rev. Lett. **52**, 1272 (1984).

[22] N. Schulz, V. Vanin, M. Aïche, A. Chevallier, J. Chevallier, J. C. Sens, Ch. Briancon, S. Ćwiok, E. Ruchowska, J. Fernandez-Niello, Ch. Mittag, and J. Dudek, Phys. Rev. Lett. **63**, 2645 (1989).

[23] V. M. Strutinsky, Nucl. Phys. A **95**, 420 (1967); **122**, 1 (1968).

[24] M. Brack, J. Damgaard, A. S. Jensen, H. C. Pauli, V. M. Strutinsky, and C. Y. Wong, Rev. Mod. Phys. **44**, 320 (1972).

[25] A. Gaamouci, I. Dedes, J. Dudek, A. Baran, N. Benhamouda, D. Curien, H. L. Wang, and J. Yang, Phys. Rev. C **103**, 054311 (2021).

[26] The *universal Woods-Saxon Hamiltonian* and associated, so-called universal parametrization has been developed in a series of articles: J. Dudek and T. Werner, J. Phys. G: Nucl. Phys. **4**, 1543 (1978); J. Dudek, A. Majhofer, J. Skalski, T. Werner, S. Cwiok, and W. Nazarewicz, *ibid.* **5**, 1359 (1979); J. Dudek, W. Nazarewicz, and T. Werner, Nucl. Phys. A **341**, 253 (1980); J. Dudek, Z. Szymański, and T. Werner, Phys. Rev. C **23**, 920 (1981), and has been summarized in S. Ćwiok, J. Dudek, W. Nazarewicz, J. Skalski, and T. Werner, Comput. Phys. Commun. **46**, 379 (1987). This approach is being used without modifications by many authors also today.

[27] To illustrate of the use frequency of the "universal' Woods-Saxon phenomenological mean-field Hamiltonian we quote below the articles which appeared only in one year (2013) and only in one journal: J. Rissanen, R. M. Clark, K. E. Gregorich, J. M. Gates, C. M. Campbell, H. L. Crawford *et al.*, Phys. Rev. C **88**, 044313 (2013); W. Brodziński and J. Skalski, *ibid.* **88**, 044307 (2013); S. Lalkovski, A. M. Bruce, A. M. Denis Bacelar, M. Górska, S. Pietri, Z. Podolyak *et al.*, *ibid.* **88**, 024302 (2013); H. L. Liu and F. R. Xu, *ibid.* **87**, 067304 (2013); D. S. Delion and R. J. Liotta, *ibid.* **87**, 041302(R) (2013); D. S. Delion, R. J. Liotta, and R. Wyss, *ibid.* **87**, 034328 (2013); D. S. Delion and J. Suhonen, *ibid.* **87**, 024309 (2013); D. Deleanu, D. L. Balabanski, T. Venkova, D. Bucurescu, N. Marginean, E. Ganioglu *et al.*, *ibid.* **87**, 014329 (2013).

[28] J. Dudek, B. Szpak, M.-G. Porquet, H. Molique, K. Rybak, and B. Fornal, J. Phys. G: Nucl. Part. Phys. **37**, 064031 (2010).

[29] The Editors, Phys. Rev. A **83**, 040001 (2011).

[30] H. J. Krappe, J. R. Nix, and A. J. Sierk, Phys. Rev. C **20**, 992 (1979).

[31] P. Möller and J. R. Nix, Nucl. Phys. A **361**, 117 (1981).

[32] P. Möller and J. R. Nix, At. Data Nucl. Data Tables **26**, 165 (1981).

[33] P. Möller, J. R. Nix, W. D. Myers, and W. J. Swiątecki, At. Data Nucl. Data Tables **59**, 185 (1995).

[34] I. Hamamoto, B. Mottelson, H. Xie, and X. Z. Zhang, Z. Phys. D: At. Mol. Clusters **21**, 163 (1991).

[35] A. Bohr and B. R. Mottelson, *Nuclear Structure* (W. A. Benjamin, Reading, MA, 1975), Vol. 2.

[36] P. A. Butler, J. Phys. G: Nucl. Part. Phys. **43**, 073002 (2016).

[37] S. C. Pancholi, *Pear-Shape Nuclei* (World Scientific, Publishing, Singapore, 2020).

[38] B. Pritychenko, M. Birch, B. Singh, and M. Horoi, At. Data Nucl. Data Tables **107**, 1 (2016).

[39] National Nuclear Data Center (NNDC) database, Brookhaven National Laboratory, https://www.nndc.bnl.gov/

[40] D. Rouvel and J. Dudek, Phys. Rev. C **99**, 041303(R) (2019).

[41] J. Dudek, A. Góźdź, and D. Rosły, Acta Phys. Pol. **32**, 2625 (2001).

[42] A. Góźdź, M. Miśkiewicz, and J. Dudek, Int. J. Mod. Phys. **17**, 272 (2008).

[43] K. T. Hecht, J. Mol. Spectrosc. **5**, 355 (1961).

[44] W. G. Harter and D. E. Weeks, J. Chem. Phys. **90**, 4727 (1989).

[45] P. Ring and P. Schuck, *The Nuclear Many-Body Problem* (Springer, New York, 1980).

[46] J.-P. Blaizot and G. Ripka, *Quantum Theory of Finite Systems* (MIT Press, Cambridge, MA, 1985).

[47] M. Bender, P.-H. Heenen, and P.-G. Reinhard, Rev. Mod. Phys. **75**, 121 (2003).

[48] E. B. Wilson Jr., J. Chem. Phys. **3**, 276 (1935).

[49] G. Herzberg, *Molecular Spectra and Molecular Structure, Vol. II, Infrared and Raman Spectra of Polyatomic Molecules* (D. Van Nostrand, New York, 1945).

[50] G. Herzberg, *Molecular Spectra and Molecular Structure, Vol. III, Electronic Spectra and Electronic Structure of Polyatomic Molecules* (D. Van Nostrand, New York, 1966).

[51] N. Onishi and R. K. Sheline, Nucl. Phys. A **165**, 180 (1971).

[52] D. Robson, Nucl. Phys. A **308**, 381 (1978).

[53] D. Robson, Phys. Rev. Lett. **42**, 876 (1979).

[54] D. Robson, Phys. Rev. C **25**, 1108 (1982).

[55] D. J. Marín-Lámbarri, R. Bijker, M. Freer, M. Gai, Tz. Kokalova, D. J. Parker, and C. Wheldon, Phys. Rev. Lett. **113**, 012502 (2014).

[56] R. Bijker and F. Iachello, Nucl. Phys. A **957**, 154 (2017).

[57] M. Hamermesh, *Group Theory and Its Application to Physical Problems* (Dover, New York, 1962).

[58] G. F. Koster, J. O. Dimmock, R. G. Wheeler, and H. Statz, *Properties of the Thirty-Two Point Groups*, (MIT Press, Cambridge, MA, 1963).

[59] J. F. Cornwell, *Group Theory in Physics – An Introduction* (Academic, New York, 1997).